

Fuel-Optimal Collision Avoidance Maneuvers in Long-Term Encounters with Station-Keeping Constraints

Zeno Pavanello^{*}, Laura Pirovano[†] and Roberto Armellin[‡]

Te Pūnaha Ātea - Space Institute, The University of Auckland, Auckland, New Zealand, 1010

This work presents a method to compute fuel-optimal collision avoidance maneuvers for long-term encounters. The fuel-optimal problem is formulated as a sequential convex program employing successive convexification of the dynamics and a projection and linearization algorithm to convexify the keep-out zone constraint. Dealing with the long-term conjunction poses additional challenges w.r.t. the short-term problem because the encounter is not instantaneous. Thus, the collision avoidance (CA) constraint is formulated as a continuous condition to be respected throughout the time frame of interest. The robustness of the solution is improved by the introduction of a condition on the sensitivity of the collision metric. Furthermore, the CA problem is coupled with the classical station-keeping requirement for GEO satellites and with a return to the nominal orbit condition for LEO satellites. A new trust region definition is employed to mitigate the effect of the linearization of the dynamics. The proposed approach calculates optimal solutions for many initial conditions and different orbital scenarios. The optimizer only takes a few seconds to find a solution, making the method suitable for autonomous calculations.

I. Introduction

The space population is rapidly increasing. As of the end of 2022, more than 32,000 objects larger than 10 cm are being tracked in space, and the active space population has doubled in the last four years [1]. The increase in the number of operational spacecraft is mainly due to miniaturization (e.g., CubeSats) and the launch of mega-constellations (e.g., Starlink). In parallel, the number of tracked space debris is growing thanks to improved monitoring systems (e.g., the space fence system). This situation brings new challenges in space situational awareness and spacecraft operations.

One of these is the risk of collision between space objects. The probability of a conjunction event occurring increases with the increasing density of the orbital regime [2], as indicated by research conducted in both low Earth orbit (LEO) [3] and geostationary Earth orbit (GEO) [4]. In recent times, there has been a significant increase in research focus on collision avoidance (CA) in order to tackle this issue. In particular, the development of autonomous and fuel-optimized

^{*}PhD candidate.

[†]Research Fellow.

[‡]Associate Professor.

collision avoidance maneuvers (CAMs) aims to effectively decrease operational expenses, minimize reliance on human intervention, and extend the lifespan of missions by mitigating propellant wastage. Conjunction events are typically considered too risky when the probability of collision (P_C) is greater than an arbitrary threshold. NASA identifies two such thresholds, corresponding respectively to the yellow and the red warning: the former is 10^{-5} , and the latter is 10^{-4} [5]. When these limits are exceeded, a CAM is designed to lower the value of P_C while respecting operational constraints, if required.

Conjunctions can be divided into two major types: short-term and long-term. The former is the most common and has been investigated more thoroughly. In this circumstance, the relative velocity involved is high, and the collision is almost instantaneous: the conjunction dynamics can be approximated as linear without loss of accuracy, and the event is studied on the two-dimensional B-plane [6–8]. In long-term conjunctions, the two objects move on similar orbits, and the event cannot be considered instantaneous [9]. This feature renders the risk quantification and, consequently, the design of CAMs more complex. Chan [10] showed that a simple condition to catalog conjunction as short-term is that the path of relative motion may be considered a straight line over a distance of 8 – 25 km with a deviation lower than 2 m. Dolado *et al.* [11], instead, identify a hard demarcation limit based on the relative velocity at time of closest approach (TCA): a conjunction is short-term if the relative velocity is higher than 10 m/s; they also propose a weaker limit at 5 m/s. CAM strategies that involve long-term encounters need to consider certain limitations, such as the higher computational requirement and the impracticality of computing P_C [12], which is typically substituted by other collision indicators, such as the instantaneous probability of collision (P_{IC}).

CA strategies have been developed for long-term encounters in terms of linear program (LP) [13] and deterministic disjunctive LP [14]. Although elegant and typically fast, the relative dynamics models of LP formulations are simplified, and the optimization may recover a solution far from the original nonlinear problem. Moreover, the solution’s optimality is also affected by using the 1-norm of the sum of the control history.

This paper investigates a convex formulation of the problem to mitigate current limitations. The use of convex optimization to solve trajectory design problems is particularly appealing as it has been proven to be efficient for many applications [15], from short-term CAMs [7, 16] to asteroid landing [17], drone formation flying [18] or spacecraft maneuver estimation [19]. Building on previous research on short-term encounters [7], this work extends it to the long-term encounters CA by introducing the linearization and projection algorithm into the 3D space. Furthermore, unlike in the short-term encounter case, the CA constraints are applied to the whole window of interest and not only at the nominal conjunction time. To guarantee a robust solution, a novel constraint is introduced to limit the sensitivity of the P_{IC} to state uncertainties. As a result, safety is ensured even in the presence of thrust misalignment or guidance, navigation, and control errors. Moreover, station keeping (SK) constraints are introduced both for GEO and for LEO orbits. In the first case, recalling the work from Mueller *et al.* [20], a linearised keep-in-box constraint bounds the spacecraft to respect a latitude-longitude requirement; in LEO a constraint on the final state forces the spacecraft to

return to its nominal orbit. The proposed method employs automatic linearization of high-fidelity dynamics and lossless relaxation to formulate a minimum fuel CAM in the form of a second-order cone program (SOCP).

The article is organized into five sections. In Section II, the dynamics of the problem are presented; in the Section III, the base CAM optimization problem is posed as a sequential convex program (SCP), and the sensitivity constraint on the collision metric is introduced. The SK constraints are introduced in Section IV, leading to the final formulation of the convex problem in Section V. The algorithm is then applied to realistic LEO and GEO test cases and conclusions are drawn in Sections VI and VII respectively.

II. Long-term Encounter Collision Dynamics

Let the state of two spacecraft (primary and secondary) be described at time t_0 by two uncorrelated Gaussian multivariate random variables

$$\mathbf{x}_p(t_0) \sim \mathcal{N}(\boldsymbol{\zeta}_p(t_0), \mathbf{C}_p(t_0)) \text{ and } \mathbf{x}_s(t_0) \sim \mathcal{N}(\boldsymbol{\zeta}_s(t_0), \mathbf{C}_s(t_0)), \quad (1)$$

where $\mathbf{x}_p(t_0), \mathbf{x}_s(t_0) \in \mathbb{R}^6$ are the two uncorrelated random variables, $\boldsymbol{\zeta}_p(t_0), \boldsymbol{\zeta}_s(t_0) \in \mathbb{R}^6$ are their mean values and $\mathbf{C}_p(t_0), \mathbf{C}_s(t_0) \in \mathbb{R}^{6 \times 6}$ are their covariance matrices. The control acceleration acting on the primary satellite is $\mathbf{u}(t) \in \mathbb{R}^3$. The state of the two objects can be numerically propagated using an arbitrary dynamics model, generally described as

$$\dot{\mathbf{x}}_p(t) = \mathbf{f}_p(t, \mathbf{x}_p(t), \mathbf{u}(t), \mathbf{p}_p) \text{ and } \dot{\mathbf{x}}_s(t) = \mathbf{f}_s(t, \mathbf{x}_s(t), \mathbf{p}_s), \quad (2)$$

where $t \in \mathbb{R}_{[t_0, t_f]}$ is the continuous time domain, $\mathbf{p}_p \in \mathbb{R}^{m_p}$ and $\mathbf{p}_s \in \mathbb{R}^{m_s}$ are sets of parameters, $\mathbf{f}_p(\cdot) : \mathbb{R}_{[t_0, t_f]} \times \mathbb{R}^6 \times \mathbb{R}^3 \times \mathbb{R}^{m_p} \rightarrow \mathbb{R}^6$ and $\mathbf{f}_s(\cdot) : \mathbb{R}_{[t_0, t_f]} \times \mathbb{R}^6 \times \mathbb{R}^{m_s} \rightarrow \mathbb{R}^6$ are continuous functions. The Gaussian nature of the variables is preserved if the nonlinearities are limited within the considered uncertainty set, e.g., when the propagation window is short enough [21].

To define the CA constraint, the relative position of the primary w.r.t. the secondary must be made explicit. Assuming that the dynamics are described using an arbitrary set of elements, which can be different from the Cartesian one, the position of the primary in ECI is a function of the state (and the same is true for the secondary):

$$\mathbf{r}_p(t) = \mathbf{h}(t, \mathbf{x}_p(t)) \quad i \in [0, N], \quad (3)$$

where $\mathbf{h}(\cdot) : \mathbb{R} \times \mathbb{R}^6 \rightarrow \mathbb{R}^3$ is a transformation that preserves the Gaussian nature of the state. It follows that $\mathbf{r}_p(t) \sim \mathcal{N}(\boldsymbol{\mu}_p(t), \mathbf{P}_p(t))$ and $\mathbf{r}_s(t) \sim \mathcal{N}(\boldsymbol{\mu}_s(t), \mathbf{P}_s(t))$. The relative position is then simply the subtraction of the two normally distributed random variables $\mathbf{r}_{rel}(t) = \mathbf{r}_p(t) - \mathbf{r}_s(t)$. Given that the subtraction is a linear transformation, also the relative position is normally distributed

$$\mathbf{r}_{rel}(t) \sim \mathcal{N}(\boldsymbol{\mu}(t), \mathbf{P}(t)), \quad (4a)$$

$$\boldsymbol{\mu}(t) = \boldsymbol{\mu}_p(t) - \boldsymbol{\mu}_s(t), \quad (4b)$$

$$\mathbf{P}(t) = \mathbf{P}_p(t) + \mathbf{P}_s(t). \quad (4c)$$

A. Collision Avoidance Optimal Control Problem

The original CA optimal control problem (OCP) in the continuous domain is stated as follows

$$\min_{\mathbf{u}} \quad J = \int_{t_0}^{t_f} u(t) dt \quad (5a)$$

$$\text{s.t.} \quad \dot{\mathbf{x}} = \mathbf{f}(\mathbf{x}(t), \mathbf{u}(t), t) \quad (5b)$$

$$P_C(\mathbf{x}(t), t) \leq \bar{P}_C \quad (5c)$$

$$\mathbf{x}(t_0) = \mathbf{x}_0 \quad (5d)$$

$$u(t)^2 = u_1(t)^2 + u_2(t)^2 + u_3(t)^2 \quad (5e)$$

$$u(t) \leq u_{max} \quad (5f)$$

where $\mathbf{u}(t) = [u_1(t) \ u_2(t) \ u_3(t)]^T$. In Problem 5, Eq. (5a) is the fuel minimization objective function, Eq. (5b) is the dynamics constraint, Eq. (5c) is the collision avoidance constraint, Eq. (5d) is the initial state bound, Eq. (5e) is a non-convex equality constraint on the control variable and Eq. (5f) is the bound on the maximum value of the control action. The mass loss due to the maneuver is not considered in the equations of motion because it is deemed negligible [7].

B. Discretization of the Dynamics

The first step towards the SOCP formulation is the discretization of Problem 5. The continuous time variable $t \in \mathbb{R}_{[t_0, t_f]}$ is substituted by the discrete time variable $t_i \in [t_0, t_1, \dots, t_N]$, where $N + 1$ is the number of equally spaced nodes of the discretization. Following Eq. (2) and via the use of an integration scheme, one obtains the states of the two spacecraft at node $i + 1$, which depend on the state and the control at node i :

$$\mathbf{x}_{p,i+1} = \mathbf{f}_{p,i}(t_i, \mathbf{x}_{p,i}, \mathbf{u}_i, \mathbf{p}_p) \quad i \in [0, N - 1], \quad (6a)$$

$$\mathbf{x}_{s,i+1} = \mathbf{f}_{s,i}(t_i, \mathbf{x}_{s,i}, \mathbf{p}_s) \quad i \in [0, N - 1], \quad (6b)$$

where $\mathbf{f}_{p,i}(\cdot), \mathbf{f}_{s,i}(\cdot) : \mathbb{R}_{[t_0, t_f]} \times \mathbb{R}^6 \times \mathbb{R}^3 \times \mathbb{R}^{m_s} \rightarrow \mathbb{R}^6$ are the discrete functions that describe the dynamics at node i , $\mathbf{x}_{p,i} = \mathbf{x}_p(t_i)$, $\mathbf{x}_{s,i} = \mathbf{x}_s(t_i)$ and $\mathbf{u}_i = \mathbf{u}(t_i)$. The differential algebra (DA) tool is used to introduce perturbations on the primary state ($\mathbf{x}_{p,i} + \delta\mathbf{x}_{p,i}$) and acceleration ($\mathbf{u}_i + \delta\mathbf{u}_i$) at each node, effectively expressing Eq. (6a) through Taylor polynomials:

$$\mathbf{x}_{p,i+1} = \mathcal{T}_{\mathbf{x}_{p,i+1}}^q(\mathbf{x}_{p,i}, \mathbf{u}_i) \quad i \in [0, N-1], \quad (7)$$

where in general the expression $\mathcal{T}_y^q(x)$ indicates the q^{th} -order Taylor expansion of the variable y as a function of x , around the expansion point \tilde{x} in which the polynomial is computed. The reader can find a detailed explanation of the use of DA in [22].

C. Selection of the Risk Metric

Probability-based criteria are the most widely employed indicators to assess the likelihood of a collision [23]. Nonetheless, many operators adopt a miss-distance strategy that only relies on the objects' mean state, so no information about the uncertainty is used. In this work, the use of three distinct metrics is analyzed, namely the instantaneous probability of collision (P_{IC}), the maximum instantaneous probability of collision ($P_{IC,m}$), and the miss distance (d_{miss}).

The most common metric used to formulate the CA condition in the short-term CA optimization problem is P_C . Typically an upper limit is set on this variable so that at TCA $P_C < \bar{P}_C$. When considering the long-term problem, the integral formula for the computation of P_C must consider the uncertainty in the position and velocity of the two space objects [24]. Moreover, this metric is highly nonlinear, thus unsuitable for a convex formulation. An alternative approach consists in setting a limit on P_{IC} rather than on P_C . P_{IC} has no dependence on the velocity uncertainty, making it simpler to compute. Additionally, P_{IC} can be further simplified to the squared Mahalanobis distance (d_m^2), transforming the collision avoidance constraint into an ellipsoidal keep-out zone, as shown in the following.

The relative position of the primary w.r.t. the secondary is the subtraction of the two multivariate distributions, as in Eq. (4). The squared Mahalanobis distance is a measure of the stochastic distance between the two normal distributions:

$$d_m^2(\mathbf{r}_{rel}(t)) = \boldsymbol{\mu}(t)^T \mathbf{P}(t)^{-1} \boldsymbol{\mu}(t). \quad (8)$$

We now consider a reference frame with the three axes aligned to Earth Centered Inertial (ECI) and centered in the secondary spacecraft to simplify the calculations. The combined hard body radius (HBR) of the two spacecraft is defined as the sum of their individual HBRs, and the volume of the two objects is condensed around the primary [7]. Also, we want to assign the whole uncertainty to the secondary spacecraft. So, $\mathbf{r}_{rel}(t)$ is shifted by an amount equal to

its mean, yielding a multivariate random variable centered at the origin, corresponding to the position of the secondary

$$\mathbf{s}(t) = \mathbf{r}_{rel}(t) - \boldsymbol{\mu}(t) \sim \mathcal{N}(\mathbf{0}_3, \mathbf{P}(t)), \quad (9)$$

Note that in the new reference system, the primary position at time t is deterministic and equal to $\boldsymbol{\mu}(t)$: it will be indicated by the symbol $\mathbf{r}(t)$ in the following. The squared Mahalanobis distance in Eq. (8), then, becomes a measure of the distance of $\mathbf{r}(t)$ from the normal distribution $\mathbf{s}(t)$

$$d_m^2 = \mathbf{r}^T \mathbf{P}^{-1} \mathbf{r}, \quad (10)$$

where the argument t has been dropped for simplicity. The value of P_{IC} at the time instant t is the integral of the Probability Density Function (PDF) of $\mathbf{s}(t)$ over the sphere \mathbb{S}_{HBR} centered in \mathbf{r} and of radius equivalent to the combined HBR of the two objects [14]:

$$P_{IC} = \frac{1}{(2\pi)^{3/2} \det(\mathbf{P})^{1/2}} \iiint_{\mathbb{S}_{\text{HBR}}} e^{-\mathbf{s}^T \mathbf{P}^{-1} \mathbf{s} / 2} dV, \quad (11)$$

Analogously to Alfried and Akella's method for P_C [23], Eq. (11) can be simplified by neglecting the variation of the PDF inside the integration region. Indeed, in typical applications, the ellipsoid associated with the covariance is at least one order of magnitude larger than the hard body sphere. The PDF, then, is evaluated only in the central point of \mathbb{S}_{HBR} ($\mathbf{s} = \mathbf{r}$), obtaining

$$P_{IC} \approx \sqrt{\frac{2}{\pi \det(\mathbf{P})}} \frac{R^3}{3} e^{-d_m^2/2}, \quad (12)$$

where R is the combined HBR.

The covariance of the position might be estimated with a large margin of error; thus we might want a more conservative approach to the estimation of the collision risk. The maximum instantaneous probability of collision is computed following the same procedure that is found in [23]

$$P_{IC,m} = \frac{(\sqrt{2}R)^3}{3e^1 d_m^2 \sqrt{\pi \det(\mathbf{P})}}. \quad (13)$$

From Eq. (12) or Eq. (13), it is possible to approximate a constraint on P_{IC} or on $P_{IC,m}$ into a constraint on d_m^2 , which describes an ellipsoidal keep-out zone. Given a limit value of P_{IC} (\bar{P}_{IC}) or $P_{IC,m}$ ($\bar{P}_{IC,m}$), the corresponding

limit of d_m^2 alternatively becomes

$$\bar{d}_m^2 = -2 \ln \left(\frac{3\bar{P}_{IC}}{R^3} \sqrt{\frac{\pi \det(\mathbf{P})}{2}} \right), \quad (14a)$$

$$\bar{d}_m^2 = \frac{(\sqrt{2}R)^3}{3e^1 \bar{P}_{IC,m} \sqrt{\pi \det(\mathbf{P})}}, \quad (14b)$$

and the collision avoidance constraint at any time is stated as

$$d_m^2 \geq \bar{d}_m^2. \quad (15)$$

Lastly, if the previously mentioned miss distance criterion is used, the covariance matrix loses significance, and the limit is set directly on d_m^2 , where the miss distance is the Mahalanobis distance corresponding to $\mathbf{P} = \mathbf{I}_3$, $d_{miss} = \sqrt{\mathbf{r}^T \mathbf{r}$.

III. Successive Convex Optimization Problem

Maneuvers can be performed at N discretization nodes in the form of a constant acceleration within the segment, \mathbf{u}_i . The last node is an exception since the acceleration would not affect the solution.

The optimization variables are the states and controls at each node. Here the covariance matrix at each node is independent of the control because there is no feedback. Hence, the scalar optimization variables are 9 for each node: the six components of the state and the 3 components of the control. In the following, for clarity in the formulas, the state of the primary spacecraft will be indicated with \mathbf{x} and the relative position between the two with \mathbf{r} . The full history of state and controls are expressed with the symbols $\mathbb{x} \in \mathbb{R}^{6(N+1)}$ and $\mathbb{u} \in \mathbb{R}^{3N}$

$$\mathbb{x} = \begin{bmatrix} \mathbf{x}_0^T & \mathbf{x}_1^T & \dots & \mathbf{x}_N^T \end{bmatrix}^T \quad \text{and} \quad \mathbb{u} = \begin{bmatrix} \mathbf{u}_0^T & \mathbf{u}_1^T & \dots & \mathbf{u}_{N-1}^T \end{bmatrix}^T. \quad (16)$$

Three nonlinearity sources are present in the problem: (i) the dynamics in Eq. (7) can include polynomials up to any order; (ii) the CA constraint in Eq. (15) is a keep-out zone constraint, which is a non-convex one; (iii) the minimization of the fuel expenditure requires the use of a non-convex constraint in Eq. (5e), which must be relaxed into a convex one to build the SOCP. Three main steps are then required to formulate the CAM design as a SOCP [7]. Firstly, in Section III.A the dynamics are automatically linearized using DA, and an iterative SCP method is employed. Afterward, in Section III.C the objective function and the constraint on the control acceleration magnitude are reformulated by introducing an equivalent transformation. Lastly, in Section III.D a projection and linearization approach is used to linearize the CA constraint on d_m^2 . It would be more complicated to handle a constraint on P_{IC} since the expression is not a polynomial function of the position, and it would need a more coarse linearization than the one on d_m^2 .

A. Linearization of the Dynamics

The result of Eq. (6) can yield highly nonlinear results, which, if maintained in the formulation, render the problem non-convex. To address this, the nonlinearities are managed through successive linearizations of the dynamic equations. The original OCP is locally linearized into a convex sub-problem in the framework of a SCP. This process may require numerous iterations, referred to as *major iterations* denoted by index j . Once the optimization problem of a major iteration $j - 1$ is solved, the solution $(\mathbf{x}^{j-1}, \mathbf{u}^{j-1})$ becomes available, a column vector comprising the state and control at each node. Employing DA, this solution serves as an expansion point for constructing linear dynamics maps for iteration j . The continuity condition is enforced by requiring that the state after the propagation of node i is equal to the state before the propagation of node $i + 1$. To favor the convergence of the iterations, it is advisable to normalize the control over its maximum value so that $\mathbf{u}_i \rightarrow \mathbf{u}_i / u_{max}$ and $0 \leq \|\mathbf{u}_i\| \leq 1$. In the following, the dynamics equations need to account for the normalized control, i.e., when computing the linear maps, the control must be scaled back into its original dimensions. The state and acceleration of each node are expanded around the reference points $\tilde{\mathbf{x}}_i$ and $\tilde{\mathbf{u}}_i$

$$\mathbf{x}_i^j = \tilde{\mathbf{x}}_i^j + \delta \mathbf{x}_i^j \quad i \in [0, N - 1], \quad (17a)$$

$$\mathbf{u}_i^j = \tilde{\mathbf{u}}_i^j + \delta \mathbf{u}_i^j \quad i \in [0, N - 1], \quad (17b)$$

The state at the subsequent node is obtained through the propagation of the first-order dynamics, as in Eq. (7)

$$\mathbf{x}_{i+1}^j = \mathcal{T}_{\mathbf{x}_{i+1}^j}^1(\mathbf{x}_i^j, \mathbf{u}_i^j) \quad i \in [0, N - 1]. \quad (18)$$

The linear maps can be extracted from the first-order expansion obtained with DA. These maps establish the dynamics relationship between the perturbations before the propagation of node i and the ones after the propagation at node $i + 1$. Thus, from Eq. (18) one obtains

$$\delta \mathbf{x}_{i+1}^j = \mathbf{A}_{i+1}^j \delta \mathbf{x}_i^j + \mathbf{B}_{i+1}^j \delta \mathbf{u}_i^j \quad i \in [0, N - 1], \quad (19)$$

where $\mathbf{A}_{i+1}^j \in \mathbb{R}^{6 \times 6}$ is the state transition matrix (STM) and $\mathbf{B}_{i+1}^j \in \mathbb{R}^{6 \times 3}$ is the control-state transition matrix. Recalling Eq. (17), the continuity constraint can be written:

$$\mathbf{x}_{i+1}^j = \mathbf{A}_{i+1}^j \mathbf{x}_i^j + \mathbf{B}_{i+1}^j \mathbf{u}_i^j + \mathbf{c}_i^j \quad i \in [0, N - 1], \quad (20)$$

where \mathbf{c}_i^j is the residual of the linearization $\mathbf{c}_i^j = \bar{\mathbf{x}}_{i+1} - \mathbf{A}_{i+1}^j \tilde{\mathbf{x}}_i^j - \mathbf{B}_{i+1}^j \tilde{\mathbf{u}}_i^j$ and $\bar{\mathbf{x}}_{i+1} = \mathbf{f}_{p,i}(t_i, \tilde{\mathbf{x}}_i, \tilde{\mathbf{u}}_i)$ is the constant part

of the propagation of the state. The initial condition is fixed because the maneuver cannot alter it

$$\mathbf{x}_0^j = \mathbf{x}_0^0 \quad (21)$$

B. Propagation of the Uncertainty

It is fundamental to propagate the covariance matrices of the two spacecraft throughout the trajectory so that $\mathbf{C}_{p,i}^j$ and $\mathbf{C}_{s,i}$ are associated with each node. The initial covariance of the primary spacecraft is propagated through the use of the STM

$$\mathbf{C}_{p,i+1}^j = \mathbf{A}_{i+1}^j \mathbf{C}_{p,i}^j (\mathbf{A}_{i+1}^j)^T \quad i \in [0, N-1]. \quad (22)$$

Analogously, using DA, the node-wise STMs of the secondary spacecraft can be obtained, which can be used to propagate its covariance. In this second case, the STMs are independent of the optimization, and so they are constant throughout the major iterations. The covariance of the Cartesian position of the primary spacecraft is obtained using the Jacobian of the nonlinear transformation from Eq. (3)

$$\mathbf{P}_{p,i} = \mathbf{H}_{p,i} \mathbf{C}_{p,i} \mathbf{H}_{p,i}^T \quad i \in [0, N]. \quad (23)$$

where the Jacobian $\mathbf{H}_{p,i} \in \mathbb{R}^{3 \times 6}$ can be obtained using a first-order DA expansion. Equation (23) is valid for the secondary.

Since the assumption is for the states to be Gaussian, the covariance of the Cartesian relative position at each node is the sum of the covariances of the Cartesian position of the two spacecraft

$$\mathbf{P}_i^j = \mathbf{P}_{p,i}^j + \mathbf{P}_{s,i} \quad i \in [0, N]. \quad (24)$$

This 3×3 matrix defines a 3D ellipsoid that evolves in time and is pivotal in the computation of d_m^2 and thus in the definition of the CAM scheme. We stress the importance of updating the history of the covariance matrices of the primary spacecraft with each major iteration since a specific maneuver could change more or less significantly the state transition between two nodes, leading to a different covariance. According to Eq. (10), this could cause a d_m^2 constraint to be violated in the node, thus requiring a different maneuver w.r.t. the previous major iteration.

C. Lossless relaxation

Equation (5e) is a non-convex equality constraint. In [25] a lossless relaxation is introduced on a similar constraint. Equation (5e) is relaxed by the introduction of the inequality sign, so that it turns into a second-order cone constraint. The variable u_i is now allowed to take values higher than the norm of the control that acts on the dynamics, and is thus

called *slack input*

$$u_i \geq \sqrt{u_{i,1}^2 + u_{i,2}^2 + u_{i,3}^2} \quad i \in [0, N-1], \quad (25)$$

The discretized forms of Eq. (5a) and Eq. (5f) become respectively

$$J = \sum_{i=0}^{N-1} u_i, \quad (26)$$

$$0 \leq u_i \leq 1 \quad i \in [0, N-1], \quad (27)$$

This relaxation of the objective function is lossless, meaning that the optimal solution for the convexified problem is also optimal for the original problem.

D. Projection Convex Sub-Problem and Linearization of the CA Constraint

The primary goal of the optimization process is to reduce the collision risk by minimizing P_{IC} . This objective is mathematically formulated in Section III.D.1 using d_m^2 by leveraging the method proposed by Mao et al.[26] and Armellin [7]. In Section III.E, the formulation is made more robust by introducing a sensitivity constraint acting on the gradient of d_m^2 .

A projection and linearization algorithm is utilized to convexify the nonlinear constraint in Eq. (15), as depicted in Figure 1. This algorithm operates iteratively within the framework of minor iterations, denoted by the symbol k . For each node, the projection convex sub-problem aims to find the point on the surface of an ellipsoid that is closest to the relative position $\mathbf{r}_i^{j,k-1}$ from the previous minor iteration. When $k = 1$, the value of $\mathbf{r}_i^{j,0}$ is the value of the last minor iteration of the previous major iteration. Additionally, if $j = 1$, $\mathbf{r}_i^{1,0}$ is the position of node i of the ballistic trajectory. In the formulation of the convex sub-problem, the indices i and j are dropped since one of these problems is solved

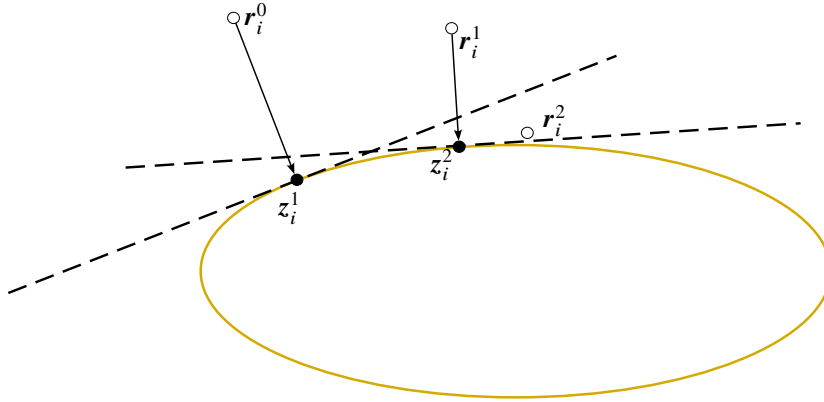


Figure 1 Simplified minor iterations in 2D.

multiple times inside the same major iteration and for each node.

1. Linearization of the Squared Mahalanobis Distance Constraint

Before solving the problem, it is convenient to diagonalize the covariance matrix. Let the dynamics used in the major convex problem be expressed in the \mathcal{B} reference frame (e.g., an ECI frame), then $\mathbf{r}_{\mathcal{B}}^{k-1} \in \mathbb{R}^3$ and $\mathbf{P}_{\mathcal{B}} \in \mathbb{R}^{3 \times 3}$ are respectively the mean value and the covariance matrix of the relative position multivariate random variable expressed in this frame. Since the covariance matrix is symmetric positive semi-definite, its eigenvalues are real and non-negative. The eigenvalues are arranged in a column vector $\boldsymbol{\lambda} = [\lambda_1 \ \lambda_2 \ \lambda_3]^T$, while the corresponding eigenvectors in the matrix $\mathbf{V} = [\mathbf{v}_1 \ \mathbf{v}_2 \ \mathbf{v}_3]$. By taking the transpose of \mathbf{V} , denoted as \mathbf{V}^T , the relative position can be rotated into a new reference system \mathcal{C} . In this new reference system, the covariance matrix becomes diagonal

$$\mathbf{P}_{\mathcal{C}} = \mathbf{V}^T \mathbf{P}_{\mathcal{B}} \mathbf{V} = \text{diag}([\lambda_1 \ \lambda_2 \ \lambda_3]), \quad (28)$$

Similarly, the relative position vector of the previous iteration is rotated in order to be expressed in the same reference frame as the covariance matrix:

$$\mathbf{r}_{\mathcal{C}}^{k-1} = \mathbf{V}^T \mathbf{r}_{\mathcal{B}}^{k-1}, \quad (29)$$

To mitigate potential numerical difficulties that may impede the solver from finding an optimal solution, a transformation is applied to stretch and compress the covariance matrix, ultimately converting it into an identity matrix. This transformation is accomplished using the inverse of the square root of the eigenvalues matrix, denoted as $\mathbf{D} = \text{diag}([1/\lambda_1 \ 1/\lambda_2 \ 1/\lambda_3])$. The problem, thus, is rotated and scaled so that the variables involved are the identity matrix and the scaled rotated relative position:

$$\hat{\mathbf{r}}_{\mathcal{C}}^{k-1} = \mathbf{D} \mathbf{r}_{\mathcal{C}}^{k-1} \text{ and } \hat{\mathbf{P}}_{\mathcal{C}} = \mathbf{I}_3. \quad (30)$$

At this stage, it is possible to formulate a simple quadratic optimization problem

$$\min_{\hat{\mathbf{z}}_{\mathcal{C}}} \quad \|\hat{\mathbf{z}}_{\mathcal{C}}^k - \hat{\mathbf{r}}_{\mathcal{C}}^{k-1}\| \quad (31a)$$

$$\text{s.t.} \quad (\hat{\mathbf{z}}_{\mathcal{C}}^k)^T \hat{\mathbf{z}}_{\mathcal{C}}^k \leq \bar{d}_m^2, \quad (31b)$$

The objective Eq. (31a) imposes the minimizes the distance between the position of the previous iteration and the optimization variable $\hat{\mathbf{z}}_{\mathcal{C}}$. Eq. (31b) imposes a relaxed condition on the optimization variable to be inside the ellipsoid. These relaxed conditions are lossless since the minimization of the objective guarantees that the optimization vector is always positioned on the surface of the ellipsoid, maximizing the distance from its center.

Once $\hat{\mathbf{z}}_{\mathcal{C}}$ is determined, the solution is transformed back into the physical space using the equation $\mathbf{z}_{\mathcal{B}}^k = \mathbf{V} \mathbf{D}^{-1} \hat{\mathbf{z}}_{\mathcal{C}}^k$.

After obtaining $\mathbf{z}_i^{j,k} = \mathbf{z}_g^k$, a linearization of the CA constraint of Eq. (15) is applied. Specifically, the dot product between the gradient of d_m^2 computed at the point located on the ellipsoid surface and the vector going from that point to the optimized trajectory point must be positive. This ensures that the new optimized relative position lies within the hemispace defined by the plane tangent to the ellipse on $\mathbf{z}_i^{j,k}$, as shown in Fig. 1. The equation of the constraint is, then

$$\nabla(d_m^2)^{j,k} \Big|_{\mathbf{z}_i^{j,k}} \cdot (\mathbf{r}_i^{j,k} - \mathbf{z}_i^{j,k}) \geq 0 \quad i \in [1, N], \quad (32)$$

As highlighted by Malyuta et al. [27], SCP algorithms can only converge if the initial trajectory guess is feasible w.r.t. the convex constraint, even if it does not comply with the nonlinear dynamics. In other words, the method described above only works if $\hat{\mathbf{r}}_C^{k-1}$ lies outside the region occupied by the ellipsoid volume for every node. Conversely, if the original point satisfies the inequality constraint in Eq. (31b), the relaxation fails because the objective function in Eq. (31a) becomes zero when $\hat{\mathbf{z}}_C^k = \hat{\mathbf{r}}_C^{k-1}$: this leads to Eq. (32) being undefined since the value of the gradient must be computed on the surface of the ellipsoid for it to be a relevant relaxation of the nonlinear constraint. So, for the nodes in which the original point is inside the ellipsoid, one should find a starting point (at major iteration j and minor $k = 0$) that satisfy Eq. (32), before applying the projection and linearization algorithm. A straightforward approach to address this issue is to use the point of intersection between the surface of the ellipsoid and the line connecting the ellipsoid's origin with the original point as the initial expansion point. In frame C , this point can be computed as follows

$$\mathbf{r}'_C^{j,0} = \left[\left(\frac{x}{\lambda_1} \right)^2 + \left(\frac{y}{\lambda_2} \right)^2 + \left(\frac{z}{\lambda_3} \right)^2 \right]^{-\frac{1}{2}} \mathbf{r}_C^{j,0}, \quad (33)$$

where $\mathbf{r}'_C^{j,0}$ is the new point that might not satisfy the dynamics, $\mathbf{r}_C^{j,0} = [x \ y \ z]^T$ is the original point inside the ellipsoid.

E. Squared Mahalanobis Distance Sensitivity Constraint

A typical solution of the long-encounter CA problem yields a P_{IC} profile, presenting at least one local maximum that is usually very close to \bar{P}_{IC} . If the gradient of d_m^2 for these points is large, small perturbations in the solution may cause the actual value of d_m^2 to vary significantly. For this reason, it is chosen to introduce a constraint that bounds the value of the norm of the gradient of d_m^2 for these nodes.

Let us assume that a solution of a major iteration $j - 1$ is available, then $P_{IC,i}^{j-1}$ is known for every node. The constraint on the gradient of d_m^2 is applied at node i only if the following condition is respected

$$P_{IC,i}^{j-1} \geq (1 - \varepsilon) \bar{P}_{IC}, \quad (34)$$

where $\varepsilon \in \mathbb{R}_{[0,1]}$ is an arbitrary percentage of the P_{IC} limit. This constraint bounds the norm of the gradient to be

lower or equal to a certain limit λ

$$\text{if Eq. (34) is true,} \quad \|\nabla(d_m^2)_i\| \leq \gamma_i \quad i \in [1, N]. \quad (35)$$

The limit value of the gradient γ_i is computed according to the following procedure. Let the maximum allowed deviation of P_{IC} at a distance Δr (e.g. equal to the combined HBR) from \mathbf{r} be equal to or lower than a percentage of \bar{P}_{IC}

$$\Delta P_{IC, \max} \leq \rho \bar{P}_{IC}, \quad (36)$$

where $\rho \in \mathbb{R}_{[0,1]}$ is a design parameter. The P_{IC} variation can be expressed as a function of the derivative of P_{IC} w.r.t. d_m^2 and of the distance $d\mathbf{r}$ from the relative position \mathbf{r}

$$dP_{IC} = \frac{\partial P_{IC}}{\partial d_m^2} \nabla(d_m^2) \cdot d\mathbf{r}. \quad (37)$$

The derivative of P_{IC} is always negative because it is computed according to the approximation in Eq. (12)

$$\frac{\partial P_{IC}}{\partial d_m^2} = -\frac{P_{IC}}{2}. \quad (38)$$

To maximize the expression in Eq. (37), then, the deviation must be parallel and opposite to ∇d_m^2 and equal to Δr in magnitude:

$$d\mathbf{r} = -\Delta r \frac{\nabla(d_m^2)}{\|\nabla(d_m^2)\|}. \quad (39)$$

Substituting Eq. (39) and Eq. (38) into Eq. (37), one gets an explicit expression for the limit of the variation of P_{IC}

$$\bar{\Delta P}_{IC} = \frac{P_{IC}}{2} \|\nabla(d_m^2)\| \Delta r. \quad (40)$$

Now, substituting Eq. (40) into Eq. (36) and rearranging, the limit imposed to ∇d_m^2 in Eq. (35) eventually depends on the value of P_{IC}

$$\gamma_i = 2\rho \Delta r \bar{P}_{IC} / P_{IC,i} \quad i \in [1, N]. \quad (41)$$

The components of $\nabla(d_m^2)_i$ are 3 new optimization variables per node.

Since the expression of d_m^2 is quadratic w.r.t. the relative position variable \mathbf{r}_i , its gradient is linear, so it is possible to express it in the form

$$\nabla(d_m^2)_i = \mathbf{D}_i \mathbf{r}_i \quad i \in [1, N], \quad (42)$$

where $\mathbf{D}_i \in \mathbb{R}^{3 \times 3}$ is the Cholesky decomposition of the normal matrix (\mathbf{P}_i^{-1}) .

IV. Station-Keeping Constraints

The base SOCP presented in Section III is completed in this section by the translation of SK requirements into a linear constraints.

A. GEO Station-Keeping Constraint

Maneuvers GEO orbits must consider the need to respect a SK constraint. The SK is viewed as a "keep-in box" in two dimensions, the longitude and the latitude of the spacecraft. The nonlinear dynamics of the evolution of the two geodetic variables are dependent only on the state of the primary spacecraft and on the time variable

$$\phi(t) = g(t, x(t)), \quad (43)$$

where $g(\cdot) : \mathbb{R}_{[t_0, t_f]} \times \mathbb{R}^6 \rightarrow \mathbb{R}^2$ is a function that first transforms the state into Earth Centered Earth Fixed (ECEF) and then into geodetic and $\phi \in \mathbb{R}^2$ is the vector comprising latitude and longitude. After discretization, the perturbation in the state is given by Eq. (17a), where the expansion point is, as usual, the output of the previous major iteration ($\bar{x}_i^j = x_i^{j-1}$).

Using DA, Eq. (43) is approximated as a first-order Taylor polynomial

$$\phi_i^j = \mathcal{T}_{\phi_i^j}^1(x_i^j) \quad i \in [1, N]. \quad (44)$$

Equation 44 allows for the representation of the perturbation of the geodetic coordinates as a linear transformation of the perturbation of the state

$$\delta\phi_i^j = G_i^j \delta x_i^j \quad i \in [1, N], \quad (45)$$

where $G_i^j \in \mathbb{R}^{2 \times 6}$ is the linear map of the geodetic transformation for node i in major iteration j .

The SK requirement states that at all times, the latitude and longitude need to be inside a rectangular box which is centered on the nominal coordinates $\phi_0 \in \mathbb{R}^2$; the sides of the box are the elements of $\Delta\phi \in \mathbb{R}^2$

$$\phi_0 - \Delta\phi \leq \phi_i^j \leq \phi_0 + \Delta\phi \quad i \in [1, N], \quad (46)$$

where the symbol \leq indicates the componentwise inequality. Thus, rearranging Eq. (45) and Eq. (17a) and splitting the two inequalities, the linearized SK constraint can be written as two componentwise inequalities

$$G_i^j x_i^j \geq \phi_0 - \Delta\phi + d_i^j \quad i \in [1, N], \quad (47a)$$

$$G_i^j x_i^j \leq \phi_0 + \Delta\phi + d_i^j \quad i \in [1, N], \quad (47b)$$

where $\mathbf{d}_i^j = \mathbf{G}_i^j \mathbf{x}_i^{j-1} - \bar{\boldsymbol{\phi}}_i^j$ is the residual of the linearization. $\bar{\boldsymbol{\phi}}_i^j = \mathbf{g}(\tilde{\mathbf{x}}_i^j, t_i)$ is the constant part of the geodetic transformation, i.e., the nonlinear function evaluation of the expansion point.

B. Station-Keeping State Targeting

A condition of return to the nominal orbit can be implemented setting the final target state of the optimization to be equal to the final state of the ballistic trajectory. Thus, a new bound constraint is introduced into the original convex problem, which bounds the state at the last node of the optimization:

$$\mathbf{x}_N + \mathbf{s}_T^+ - \mathbf{s}_T^- = \mathbf{x}_T, \quad (48)$$

where the variables \mathbf{s}_T^+ and $\mathbf{s}_T^- \in \mathbb{R}^6$ are slack variables used to create a soft constraint, and $\mathbf{x}_T = \mathbf{x}_N^0$. A trade-off between the pure CA and the pure SK maneuvers can be obtained adding a term to the objective function. The weight κ_T determines the softness of the constraint

$$J_T = \kappa_T \|\mathbf{s}_T^+ + \mathbf{s}_T^-\|_1 \quad (49a)$$

$$\mathbf{s}_T^+, \mathbf{s}_T^- \geq 0, \quad (49b)$$

In LEO scenarios, the return to the nominal orbit can be considered a sufficient station keeping requirement, but the same is not valid for GEO orbits.

For GEO orbits, finding the target state \mathbf{x}_T to minimize the violation of the SK box is the typical optimization problem of the periodic SK maneuvers. Analytical solutions exist when only the first harmonics of the gravity potential are considered. In contrast, classical nonlinear optimization methods can solve the problem numerically when more perturbations are considered. To overcome the long computational time required by the latter method, a SCP formulation is presented, where the dynamics are dealt with using the method presented in Section III.A. The objective of the optimization is to maximize the time spent inside the SK box during a period $t \in \mathbb{R}_{[t_f, t_f+y]}$ where t_f is the final time of the CA window and y is the length of the time frame before executing another SK maneuver. The time window is discretized in the usual way into $M + 1$ equally spaced nodes. After the discretization, it is straightforward to define the dynamics constraint for the state of the satellite in a very similar way to Eq. (20). In this case, the initial state must remain unconstrained and no control is acting

$$\mathbf{x}_{i+1}^j - \mathbf{A}_{i+1}^j \mathbf{x}_i^j = \mathbf{c}_i^j \quad i \in [0, M], \quad (50)$$

Where $\mathbf{A}_{i+1}^j \in \mathbb{R}^{6 \times 6}$ is the STM and $\mathbf{c}_i^j = \bar{\mathbf{x}}_{i+1}^j - \mathbf{A}_{i+1}^j \tilde{\mathbf{x}}_i^j$ is the residual of the linearization. The SK constraint is

enforced similarly to that of Eq. (47). In this problem the control is not available in every node to adjust the position of the spacecraft, so it is unavoidable that, in a long period of propagation (e.g., two weeks), the orbital perturbations make the satellite violate the SK box. The constraint is then enforced as a soft constraint via the introduction of $2 \times (M + 1)$ vector slack variables (each comprising two elements, which influence longitude and latitude respectively), χ_i^+ and $\chi_i^- \in \mathbb{R}^2$. These variables quantify the entity of the violation of the SK box requirement over each node

$$G_i^j r_i^j + \chi_i^+ \geq \phi_0 + d_i^j - \Delta\phi \quad i \in [0, M], \quad (51a)$$

$$G_i^j r_i^j - \chi_i^- \leq \phi_0 + d_i^j + \Delta\phi \quad i \in [0, M], \quad (51b)$$

where $d_i^j = G_i^j r_i^{j-1} - \bar{\phi}_i^j$ is the usual residual of the linearization. The slack variables need to be non-negative

$$\chi_i^+, \chi_i^- \geq 0 \quad i \in [0, M], \quad (52)$$

The optimization minimizes these violations by acting only on the initial state of the propagation. Thus the objective function is

$$J_T = \sum_{i=0}^M \|\chi_i^+ + \chi_i^-\|_1, \quad (53)$$

The optimization problem can be summarized as

$$\begin{aligned} \min_{x_0} \quad & \text{Eq. (53)} && \text{Minimization of the sum of the violations} \\ \text{s.t.} \quad & \text{Eq. (50)} && \text{Dynamics constraint} \\ & \text{Eq. (51)} && \text{SK soft constraint} \\ & \text{Eq. (52)} && \text{Lower bound on the soft constraint slack variables} \end{aligned} \quad (54)$$

V. Finalization of the SOCP

In order to finalize the SOCP, a trust region algorithm combined with virtual controls is introduced.

A. Trust Region Constraint

The use of a trust region algorithm is of pivotal importance when dealing with a complexly nonlinear problem that has been linearized. The classic approach introduces a node-wise constraint that bounds the norm of the maximum deviation allowed to the state variables w.r.t. the linearization point. The radius of the trust region is usually proportional to some performance index that is related to how well the linearized dynamics represent the actual non-linear problem [27]. Here we introduce a methodology that adjusts the trust region radius for every single variable according to a

measure of its nonlinearity and uses a limited number of parameters to update the radius.

The idea for this algorithm stems from the work of Losacco *et al.* on the nonlinearity index (NLI) [28] and the one of Bernardini *et al.* on trust region [29]: a second-order Taylor expansion of the nonlinear dynamics is computed using DA. This allows one to obtain the first-order expansion of the Jacobian of the constraints w.r.t. the optimization variables (both the states and controls):

$$\mathbf{J}_i = \bar{\mathbf{J}}_i + \delta \mathbf{J}_i \quad i \in [1, N], \quad (55)$$

where $\mathbf{J}_i \in \mathbb{R}^{6 \times 9}$. From now on, in this section, the index i will be dropped for readability; still, the equations are valid for each node.

The deviation of the Jacobian is a first-order function of the deviation of the optimization variables

$$J_{uv} = \bar{J}_{uv} + \delta J_{uv} = \bar{J}_{uv} + \sum_{k=1}^9 a_{uvw} \delta x_w \quad u \in [1, 6] \quad v \in [1, 9], \quad (56)$$

where $\delta x_w = x_w - \tilde{x}_w$ is the componentwise deviation from the reference variable, which comprises both the state and the control: $w \in [1, 6]$ indicates the state components, $w \in [7, 9]$ the control.

The component-wise NLI is defined as

$$\nu_w = \sqrt{\frac{\sum_{u=1}^6 \sum_{v=1}^9 a_{uvw}^2}{\sum_{u=1}^6 \sum_{v=1}^9 \bar{J}_{uv}^2}} |\delta x_w| = \xi_w |\delta x_w|. \quad (57)$$

The variable $\xi_w \in \mathbb{R}_{\geq 0}$ is a measure of the nonlinearity of the reference solution; $\nu_w \in \mathbb{R}_{\geq 0}$ is an indicator of the nonlinearities for a variation δx_w from the reference. To allow variations within the accuracy of the linearizations, ν_w is bounded by a maximum value $\bar{\nu}$:

$$\nu_w = \xi_w |\delta x_w| \leq \bar{\nu} \quad w \in [1, 9], \quad (58)$$

Making the absolute value explicit and bringing the optimization variables to the left, Eq. (58) translates into two trust region constraints *

$$\xi_i \odot [\mathbf{x}_i^T \mathbf{u}_i^T]^T \leq \xi_i \odot [\hat{\mathbf{x}}_i^T \hat{\mathbf{u}}_i^T]^T + \bar{\nu} \cdot \mathbf{1} \quad i \in [1, N], \quad (59a)$$

$$\xi_i \odot [\mathbf{x}_i^T \mathbf{u}_i^T]^T \geq \xi_i \odot [\hat{\mathbf{x}}_i^T \hat{\mathbf{u}}_i^T]^T - \bar{\nu} \cdot \mathbf{1} \quad i \in [1, N], \quad (59b)$$

where $\xi_i = [\xi_{i1}, \xi_{i2}, \dots, \xi_{i9}]^T$, $\mathbf{1} \in \mathbb{R}^9$ is a vector of ones, and the symbol \odot indicates the Hadamard product; the

*It is important to have ξ_{iw} in the numerator, otherwise when $\xi_{iw} = 0$ (linear dynamics) the constraint would become undefined.

index i is used again to indicate the node-wise constraints. For $i = 0$ no deviation is allowed so the constraint is not set as it would be redundant with Eq. (21). For $i = N$ the Jacobian of the constraint is not defined, so the variable ξ_N is undefined. It is still possible to impose a trust region for the state at the last node by defining $\xi_N = \xi_{N-1}$. So it is assumed that the nonlinearity of the last node behaves in the same way as the penultimate.

1. Virtual Controls

The introduction of the trust region constraint can cause artificial infeasibility, so virtual controls, and virtual buffers are added to the dynamics, CA, SK, and ∇d_m^2 constraints, which improve the convergence of the method. The new constraints with virtual controls become

$$\mathbf{x}_{i+1}^j - \mathbf{A}_{i+1}\mathbf{x}_i^j - \mathbf{B}_{i+1}^j\mathbf{u}_i^j + \mathbf{v}_{dyn,i+1}^j = \mathbf{c}_i^j \quad i \in [0, N-1], \quad (60a)$$

$$\nabla(d_m^2)^{j,k} \Big|_{\mathbf{z}_i^{j,k}} \cdot (\mathbf{r}_i^{j,k} - \mathbf{z}_i^{j,k}) + v_{ca,i}^j \geq 0 \quad i \in [1, N], \quad (60b)$$

$$\mathbf{G}_i^j\mathbf{x}_i^j + \mathbf{v}_{sk,i}^j \geq \phi_0 - \Delta\phi + \mathbf{d}_i^j \quad i \in [1, N], \quad (60c)$$

$$\mathbf{G}_i^j\mathbf{x}_i^j + \mathbf{v}_{sk,i}^j \leq \phi_0 + \Delta\phi + \mathbf{d}_i^j \quad i \in [1, N], \quad (60d)$$

$$\|\nabla(d_m^2)_i\| + v_{s,i}^j \leq \gamma_i \quad i \in [1, N], \quad (60e)$$

where $\mathbf{v}_{dyn,i}^j \in \mathbb{R}^6$ is the virtual control vector, $v_{ca,i}^j \in \mathbb{R}$ is the virtual buffer for the CA constraint, $\mathbf{v}_{sk,i}^j \in \mathbb{R}^2$ is the virtual buffer for the station keeping constraint, and $v_{s,i}^j \in \mathbb{R}$ is the virtual buffer for the d_m^2 sensitivity constraint.

Ideally, the virtual controls should all go to 0 at convergence, so a second-order cone constraint is built on each node, and in the objective function, a term is added which is proportional to it; the value of the weight in the objective function should be orders of magnitude higher than the one on the control, e.g., 10^4 , to favor the penalization of the virtual control variables

$$v_i \leq \sqrt{(v_{s,i}^j)^2 + (v_{ca,i}^j)^2 + \|\mathbf{v}_{dyn,i}^j\|^2 + \|\mathbf{v}_{sk,i}^j\|^2} \quad i \in [1, N], \quad (61a)$$

$$J_{vc} = \kappa_{vc} \sum_{i=0}^N v_i, \quad (61b)$$

B. Final Form of the SOCP

The final objective function is given by the sum of Eq. (26), Eq. (49a), and Eq. (61b):

$$J = \kappa_T \|\mathbf{s}_T^+ + \mathbf{s}_T^-\|_1 + \kappa_{vc} \sum_{i=0}^N v_i + \sum_{i=0}^{N-1} u_i. \quad (62)$$

The full convex optimization problem with the novel constraints (SK and d_m^2 sensitivity) is reported in Problem 63.

$\min_{\mathbf{x}, \mathbf{u}}$	Eq. (62)	Minimization of the total Δv , virtual controls and slack variables	
s.t.	Eq. (60a)	Dynamics constraint with virtual controls	
	Eq. (60b)	CA constraint on d_m^2 with virtual buffer	
	Eq. (60c) and Eq. (60d)	SK constraint with virtual buffers	
	Eq. (42)	∇d_m^2 definition constraint	
	Eq. (25)	Control acceleration second-order cone	
	Eq. (21)	Bound on the initial state	(63)
	Eq. (48)	Bound on the final state	
	Eq. (27)	Bound on the control acceleration cone	
	Eq. (49b)	Bound on the the slack target variables	
	Eq. (60e)	Bound on ∇d_m^2 with virtual buffers	
	Eq. (59)	Trust region bound	
	Eq. (61a)	Virtual control second-order cone	

In Algorithm 1, a high-level description of the full SCP algorithm is presented.

VI. Results

In this section, the method is applied to a LEO and a GEO scenario: the effect of different parameters and constraints is analyzed to determine how they affect the computed optimal CAM thrust profile. In particular, we will analyze the following factors: length of the CA window, risk metric, maximum thrust, and inclusion of operational constraints (SK and ∇d_m^2). The simulations are run with MATLAB r2022b on AMD Ryzen 9 6900HS @ 3.3GHz. The optimization is performed using MOSEK 10.0.24, which implements a state-of-the-art primal-dual interior point solver. The dynamics equations are propagated using the numerical propagator Accurate Integrator for Debris Analysis (AIDA) [30], which implements all the relevant orbital perturbations, such as high-order gravitational harmonics (10 orders), third body attraction of the Sun and Moon, atmospheric drag with NRLMSISE-00 density model, and solar radiation pressure (SRP).

Despite the algorithm working with the control acceleration, it was chosen to display the corresponding Δv in the figures, as it is an easier-to-understand quantity, and the mass loss due to the propulsion is neglected. The Δv is obtained by integrating the acceleration over the time step: $\Delta v_i = \mathbf{u}_i \Delta t$.

Algorithm 1 High level flow of the SCP

```

1: Get inputs for the spacecraft:  $HBR, A_{drag}, C_D, A_{SRP}, C_r, \mathbf{x}_0, \mathbf{C}_0$ 
2: Assign  $t_0, \Delta t, N, u_{max}, u_{min}, \bar{P}_{IC}$  (or  $\bar{P}_{IC,m}$  or  $\bar{d}_{miss}$ ),  $\rho, \varepsilon, \bar{v}, \text{tol}_M, \text{tol}_m, j_{max}, k_{max}$ 
3:  $t \leftarrow t_0 : \Delta t : t_0 + N\Delta t$ 
4: Perform a first-order DA propagation of the secondary trajectory starting from  $\mathbf{x}_{s,0}$ .
5: for  $i = 1 : N$  do
6:    $\bar{\mathbf{x}}_{s,i} \leftarrow$  constant part of the propagation
7:    $\mathbf{A}_{s,i} \leftarrow$  linear part of the state-state propagation
8:    $\mathbf{C}_{s,i} \leftarrow \mathbf{A}_{s,i} \mathbf{C}_{s,i-1} \mathbf{A}_{s,i}^T$ 
9:    $\mathbf{P}_{s,i} \leftarrow \mathbf{H}_{s,i} \mathbf{C}_{s,i} \mathbf{H}_{s,i}^T$ 
10: end for
11:  $j \leftarrow 0$ 
12: while  $\|\mathbb{w}^j - \mathbb{w}^{j-1}\|_\infty > \text{tol}_M \wedge j < j_{max}$  do
13:    $j \leftarrow j + 1$ 
14:    $k \leftarrow 0$ 
15:   if  $j > 1$  then
16:     Perform a second-order DA propagation with control history  $\mathbb{w}^{j-1}$  and expansion points from  $\mathbb{x}^{j-1}$ .
17:   else
18:     Perform a second-order forward DA propagation with no control.
19:   end if
20:   for  $i = 0 : N$  do
21:      $\bar{\mathbf{x}}_i^j \leftarrow$  constant part of the propagation
22:      $\bar{\boldsymbol{\phi}}_i^j \leftarrow$  constant part of the geodetic coordinates
23:      $\mathbf{A}_i^j, \mathbf{B}_i^j \leftarrow$  linear part of the propagation
24:      $\mathbf{G}_i^j \leftarrow$  linear part of the geodetic coordinates transformation
25:      $\mathbf{C}_{p,i}^j \leftarrow$  Eq. (22)
26:      $\mathbf{P}_{p,i}^j \leftarrow$  Eq. (23)
27:      $\mathbf{P}_i^j \leftarrow$  Eq. (24)
28:      $\mathbf{r}_i^j \leftarrow \mathbf{r}_{p,i}^j - \mathbf{r}_{s,i}$ 
29:      $(\bar{d}_m^2)_i^j \leftarrow$  Eq. (14a) or Eq. (14b)
30:      $(d_m^2)_i^j \leftarrow$  Eq. (10)
31:      $(P_{IC})_i^j \leftarrow$  Eq. (12)
32:      $\xi_i \leftarrow$  Eq. (57)
33:     if  $(P_{IC})_i^j > (1 - \varepsilon)\bar{P}_{IC}$  then
34:        $\gamma_i \leftarrow 2\rho\Delta r\bar{P}_{IC}/(P_{IC})_i^j$ 
35:     end if
36:   end for
37:   for  $i = 1 : N \wedge (d_m^2)_i^j < (\bar{d}_m^2)_i^j$  do
38:     Find starting point on the ellipsoid's surface using Eq. (33)
39:   end for
40:   while  $(\|\mathbb{r}^{j,k} - \mathbb{r}^{j,k-1}\|_\infty > \text{tol}_m \wedge k < k_{max})$  do
41:      $k \leftarrow k + 1$ 
42:     Solve SCP Problem (63)
43:   end while
44:    $\mathbb{x}^j \leftarrow \mathbb{x}^{j,k}$ 
45:    $\mathbb{w}^j \leftarrow \mathbb{w}^{j,k}$ 
46: end while
47: Validation: Propagate forward from the initial state using the control history from the last iteration and check the highest position error w.r.t. the last major iteration.

```

A. LEO Scenario

The LEO scenario is based on a test case reported in [9], in Table 2 the orbital parameters of the two spacecraft at TCA are reported. The simulations are run for two orbital periods with TCA as the median point of the propagation; the time nodes previous to TCA are negative, and the ones after are positive. Each orbital period is discretized into 60 nodes, granting a minimum thrust arc of 3 deg and a total of 120 available thrusting opportunities.

In Eq. (64), the covariance at TCA is expressed in the radial, along-track, cross-track (RTN) reference frame of the two spacecraft; the units of measures are $[m^2]$ for position and $[s^2]$ for time

$$C_{p0} = C_{s0} = \text{diag}([2.5, 5, 2.25, 0.375, 0.125, 0.075]) \quad (64)$$

Before summing them, the two covariance matrices must be expressed in a common reference frame, e.g., ECI.

1. Comparison of Risk Metrics

The selection of different risk metrics determines different optimal maneuvers. The chosen risk thresholds are $\bar{P}_{IC} = 10^{-6}$, $\bar{P}_{IC,m} = 10^{-4}$, and $\bar{d}_{miss} = 2$ km. The propulsion system can achieve a maximum thrust of 1 N, which corresponds to a maximum acceleration of 5 mm/s². Fig. 3 makes it clear that when the P_{IC} metric is used, the computed maneuver is mostly out-of-plane, whereas it is tangential in the other two cases. The less restrictive metric in terms of total Δv is P_{IC} , which requires 255 mm/s. Indeed, the maneuver in the N direction allows the spacecraft to avoid the evolving ellipsoid over its oblate side. The $P_{IC,m}$ metric commands a total Δv of 322 mm/s. The evolution of $P_{IC,m}$ of the ballistic trajectory envelops P_{IC} , as shown in Fig. 2a, guaranteeing that the former is a very conservative estimate of the latter. The most demanding metric, instead, is d_{miss} , with a two-firings Δv of 387 mm/s: to avoid the sphere of 2 km centered in the secondary spacecraft, the tangential maneuver is the most efficient, as expected from the short-term problem [8, 31]. Most notably, as already suggested in [9], the d_{miss} metric in Fig. 2b exhibits an opposite behavior w.r.t. P_{IC} and $P_{IC,m}$: the evolution of the covariance in the probability-based criteria determines a high risk

Table 1 Base LEO case: orbit parameters at TCA.

	m [kg]	A_{drag} [m ²]	C_D [-]	A_{SRP} [m ²]	C_r [-]	HBR [m]
Primary	200	1	2.2	1	1.31	25
Secondary	50	0.05	2	0.05	1.31	7

Table 2 Base LEO case: orbit parameters at TCA.

	a [km]	e [-]	i [deg]	ω [deg]	Ω [deg]	θ [deg]
Primary	6800	0	0	0	0	0
Secondary	6802	4.42×10^{-4}	8.4×10^{-5}	1.9103	0	-1.9103

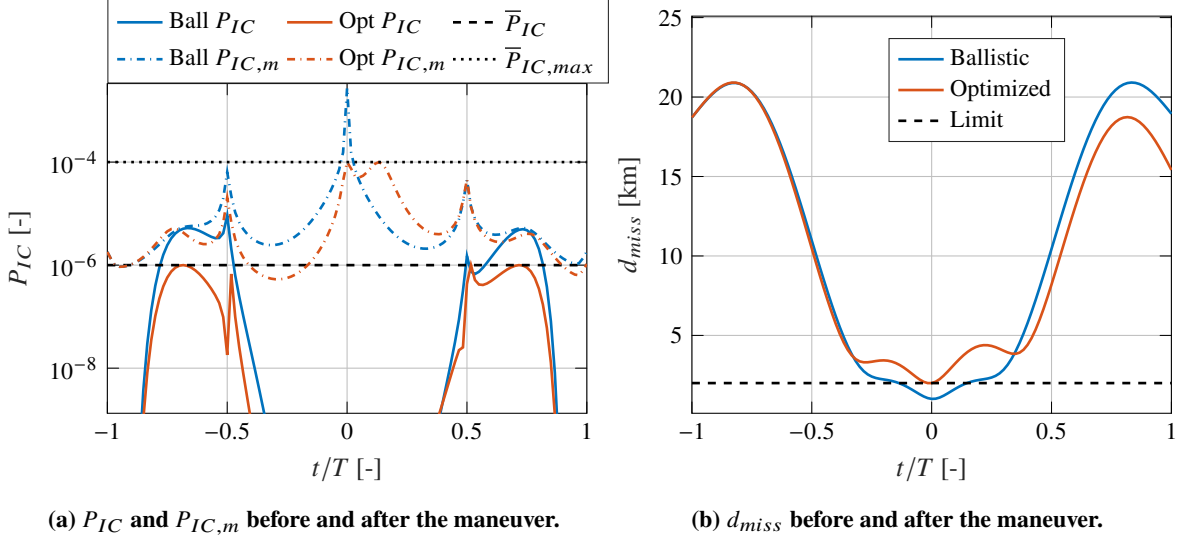


Figure 2 LEO scenario: collision metrics comparison.

in the period in which the relative distance between the two objects is higher.

2. Comparison of Thrust Systems

The same scenarios of the previous section are analyzed using a low-thrust system with a maximum thrust of 90 mN, corresponding to a maximum acceleration of 0.45 mm/s^2 . In Fig. 3 the maneuvers of the different cases are shown. In the P_{IC} case, the total Δv required is 305.3 mm/s, in the $P_{IC,m}$ case it is 325.8 mm/s and in the d_{miss} case 397.7 mm/s. The number of total nodes where thrust is active increases in the three cases from the two of the high-thrust system to 11, 14, and 15 for the low-thrust system.

3. Return to the Nominal Orbit

After completing reducing the collision risk, it might be required to the primary spacecraft to return to its nominal orbit. This is obtained by constraining the optimized final state to match the final state of the ballistic trajectory. So, in Eq. (48), $\mathbf{x}_T = \mathbf{x}_N^0$. The two trajectories, with and without return constraints, are shown in Fig. 4b. The thrust profile in Fig. 4a should be compared with the one in Fig. 3b, which is the corresponding scenario with no return constraint. The first impulse is substantially the same, with only a slight modification in the direction of the thrust (radial and along-track components). All of the following firings are used to reroute the spacecraft toward the desired final state. The total Δv increases to 899 mm/s.

4. Squared Mahalanobis Distance Sensitivity Constraint

A scenario starting from TCA and spanning the period of 1 orbit is used to analyze the influence of the d_m^2 sensitivity constraint on the maneuver. In Fig. 5a, the P_{IC} for the cases with and without the d_m^2 sensitivity constraint are shown.

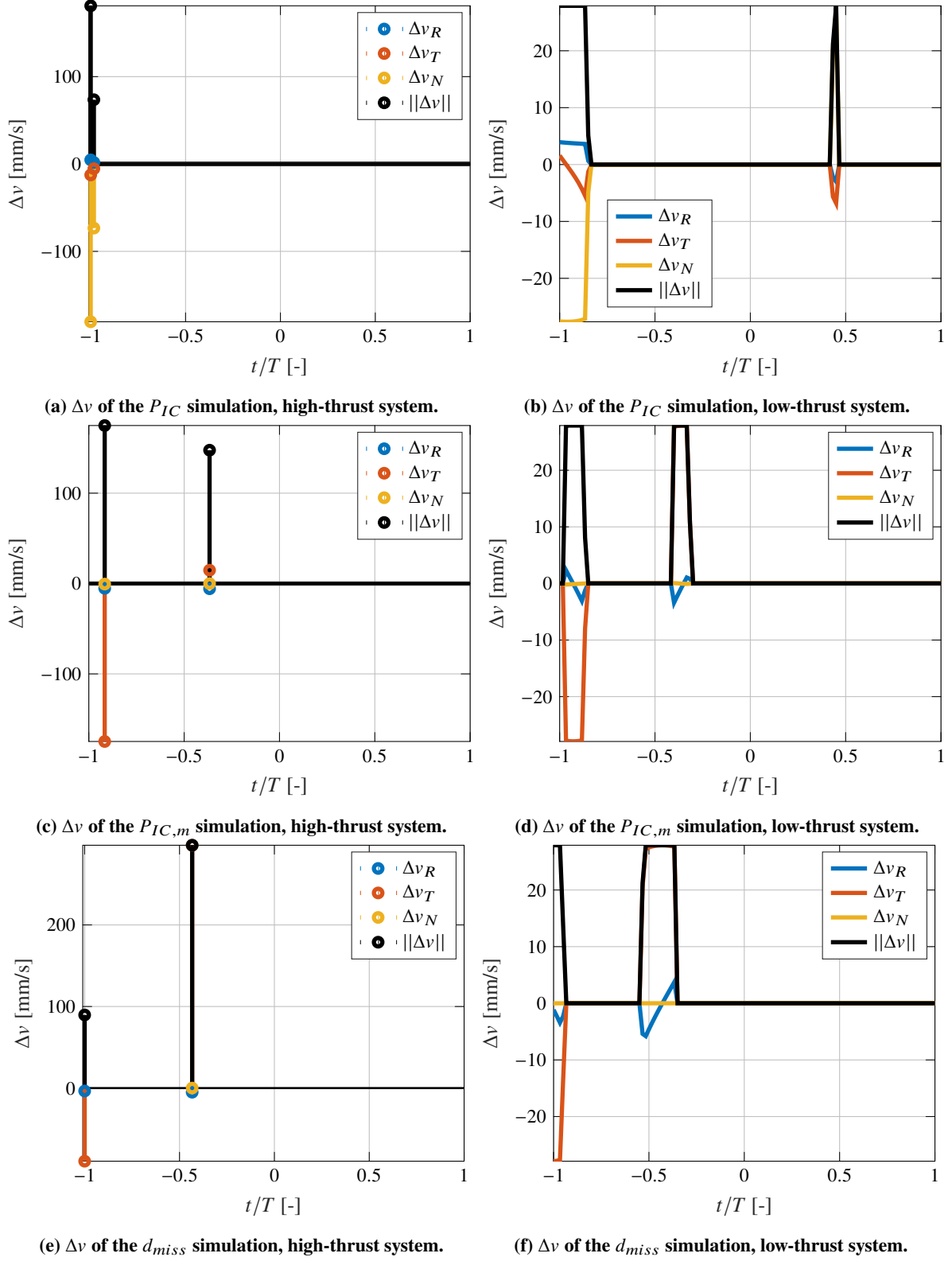


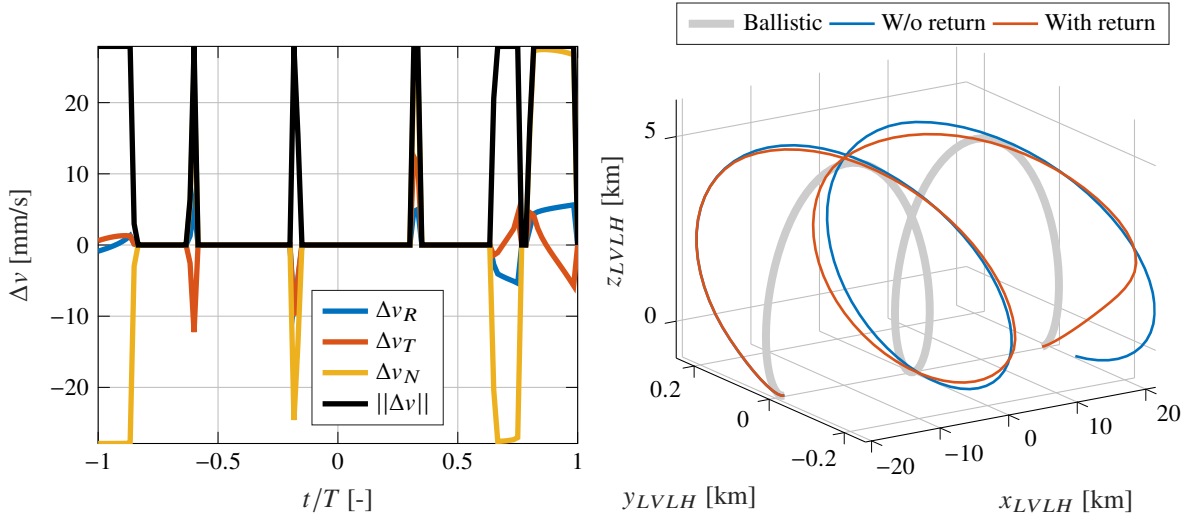
Figure 3 LEO scenario: Δv for different collision metrics and propulsion systems.

The ballistic trajectory violates the P_{IC} threshold in 15 nodes. The relative position of these nodes after the maneuver is represented in Fig. 6. To simplify the representation the relative states are plotted in a space in which the keep-out zone is a unit sphere. If $C_{I,i}$ is the combined covariance matrix at node i expressed in the ECI frame, its eigenvectors matrix V is the DCM from a reference frame oriented on the axes of the covariance and ECI; the corresponding diagonal matrix of the eigenvalues is D . The stretched and rotated relative position points in Fig. 6 are computed as

$$r_C = D^{-1} V r_I / \bar{d}_{m,i}^2. \quad (65)$$

Fig. 6 reports the trajectory obtained using 4 different $\bar{\Delta P}_{IC}$ thresholds. Decreasing the allowable deviation in terms of P_{IC} at a distance HBR in the direction of the gradient of d_m^2 , the trajectory is progressively shifted towards the semi-major axis of the ellipsoid. At the point of conjunction between the semi-major axis and the surface, the gradient of d_m^2 is minimum. In Fig. 5a a zoom of the region in which the P_{IC} of the ballistic trajectory is over the limit is shown. The maximum value of P_{IC} happens at $t/T = 0.73333$. All four maneuvers have the effect of lowering the P_{IC} maximum value to 10^{-6} ; the increasingly constraining value of $\bar{\Delta P}_{IC}$, though, bounds ΔP_{IC} to increasingly lower values. Note that the d_m^2 sensitivity constraint is applied only in $t/T = 0.73333$, since it is the only node in which P_{IC} is high enough to trigger its activation. Indeed, in Fig. 5b ΔP_{IC} computed in the direction opposite to ∇d_m^2 respects the limit in all cases. This limit is respectively 4×10^{-7} , 3×10^{-7} , 2×10^{-7} , and 10^{-7} .

The total Δv required with the constraint's introduction increases when the safety margin increases. From the unconstrained case to the case with $\rho = 0.1$, the Δv goes from 255 to 260, 378, 496, and 569 mm/s. The maneuver is always a single-impulse applied at the first node and the tangential component becomes more and more dominant.



(a) Δv of the return trajectory.

(b) Relative trajectory without and with return constraint.

Figure 4 LEO scenario: case with the return to the nominal orbit constraint.

Table 3 GEO scenario: orbit parameters at TCA.

	m [kg]	A_{SRP} [m ²]	C_r [-]	HBR [m]
Primary	500	1	1.31	35
Secondary	200	1.2	1.31	10

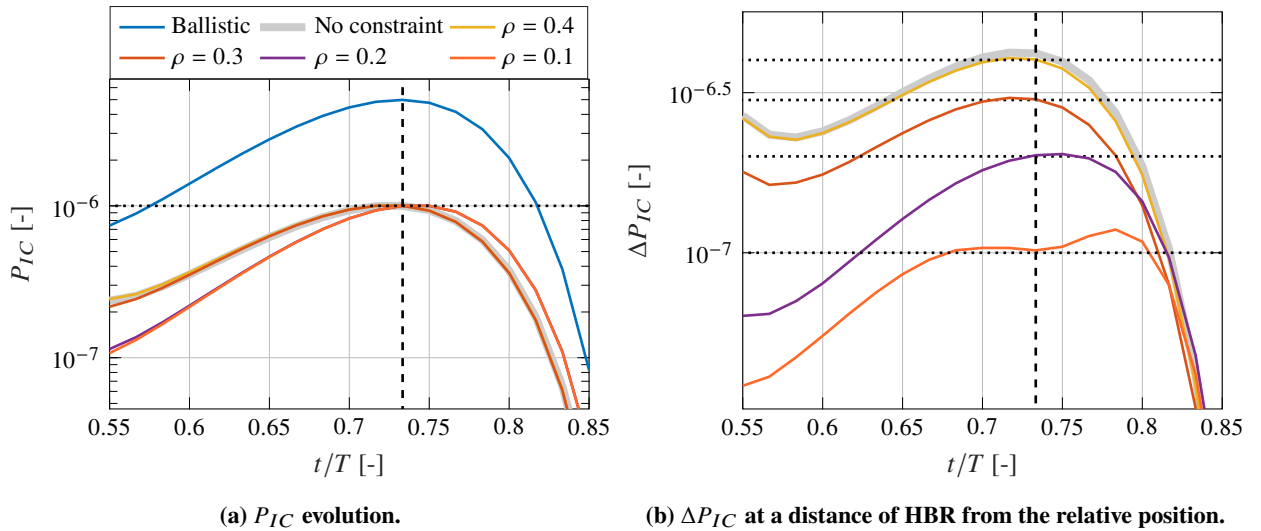
Table 4 GEO scenario: orbit parameters at TCA.

	a [km]	e [-]	i [deg]	ω [deg]	Ω [deg]	θ [deg]
Primary	42166.03	5.6×10^{-5}	0.119	241.58	76.18	119.44
Secondary	42167.76	9×10^{-5}	0.119	241.58	76.18	119.44

B. GEO Scenario

A realistic GEO test case is used to demonstrate the effectiveness of the SCP algorithm in another orbital regime. Simulations are performed considering a high thrust of 2.5 N, which corresponds to a maximum acceleration of 5 mm/s² for a 500 kg spacecraft. The orbital period is discretized into 60 nodes, so the maximum impulsive Δv between successive nodes is 7.18 m/s. For the low-thrust system the maximum thrust is 2.5 mN, i.e. a maximum acceleration of 5 μ m/s².

In Table 3, the orbital parameters of the two spacecraft at TCA are represented. The two orbits are close to a perfect GEO, with a slight inclination and a difference in the semi-major axis of 1.5 km. The covariance of the two spacecraft is the same as in Eq. (64). In Table 4 the physical properties of the spacecraft are shown. The only relevant perturbations in the GEO regime are higher order gravitational harmonics, SRP, and third body attraction, so no information is required on the equivalent drag surface area and C_D coefficient.

**Figure 5 LEO scenario: collision metrics for cases with the sensitivity constraint.**

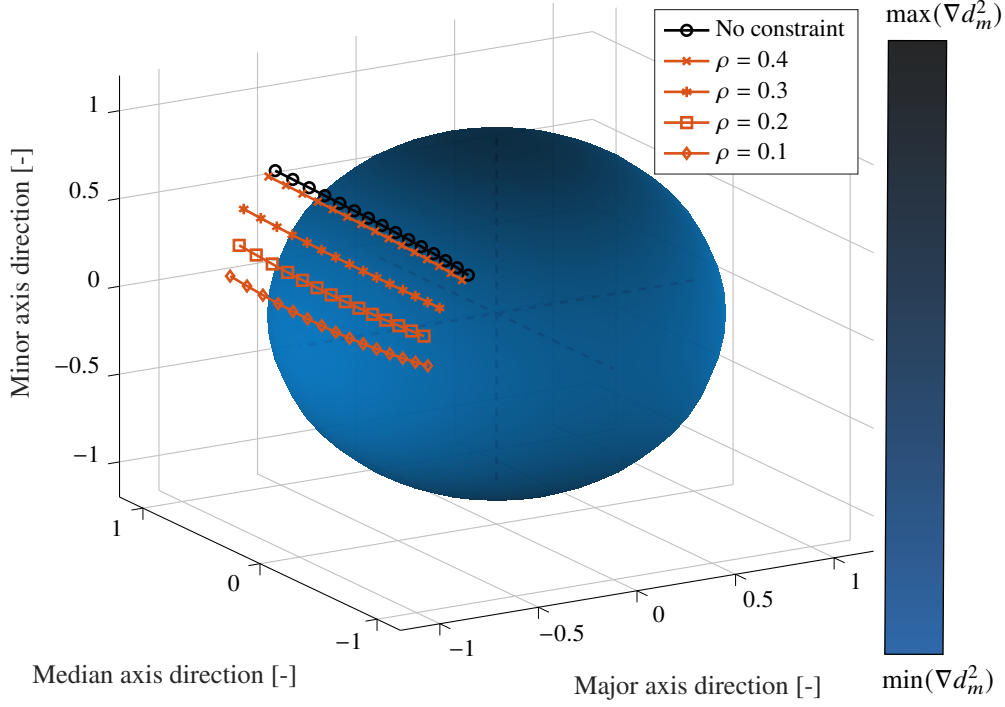


Figure 6 LEO scenario: Optimized trajectory for different values of ρ in the covariance space.

1. Station-Keeping Constraint and Targeting

The primary spacecraft is commanded to always stay inside the latitude-longitude SK square box of side $\Delta\phi = 0.05$ deg around the nominal values of latitude (0 deg) and longitude (-155.08 deg). Moreover, the optimal final state target is computed so that the SK requirement is respected by the natural motion of the satellite for the following 14 days. This requirement is respected as shown in Fig. 8. For comparison, a scenario in which the SK constraint is not enforced is also reported in Fig. 8; in that case the maneuver causes an even more serious drift on the longitude than that of the ballistic trajectory.

The SK constraint completely changes the direction of the maneuver. In fact, the SK maneuver is mostly an out-of-plane correction of the inclination, which allows keeping the latitude inside the box [32]. The pure CAM in Fig. 7b, instead, is an almost purely tangential maneuver. Also, the entity of the total Δv is significantly changed by the constraint, going from 52 mm/s in the pure CAM case to 409 mm/s in the case with SK. Given the predominance of the SK constraint, the maneuver is only slightly modified by the use of different collision metrics: Fig. 7c and Fig. 7d are very similar to Fig. 7a; the total Δv for the case with $P_{IC,m}$ is 366 mm/s and for the case with d_{miss} is 364 mm/s.

2. Squared Mahalanobis Distance Sensitivity Constraint

The d_m^2 sensitivity constraint is applied to a GEO case with no SK target. It is worth noticing from Fig. 10 that the inclusion of the constraint completely shifts the maneuver. While in Fig. 6 it is clear that progressively increasing

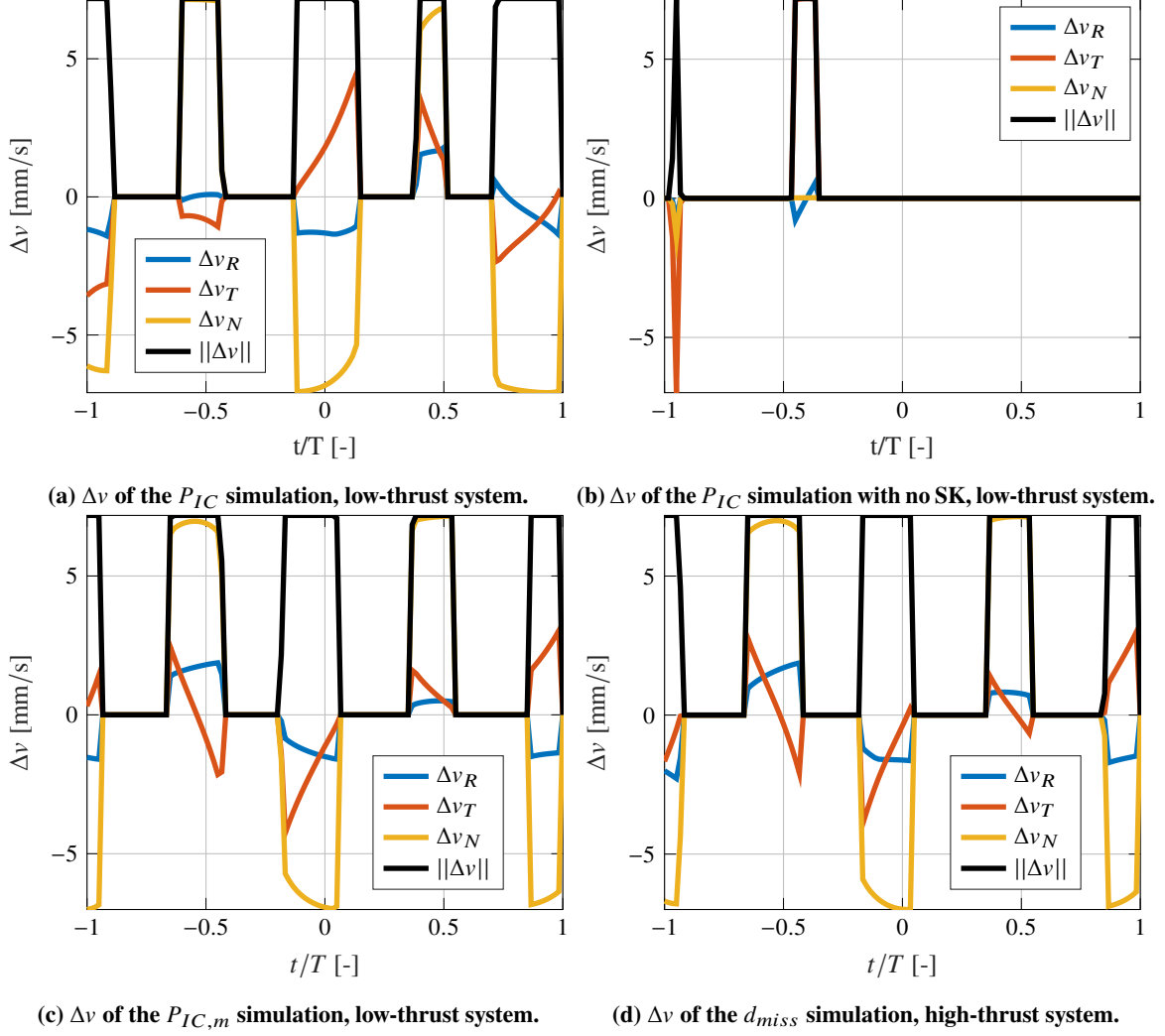


Figure 7 GEO Scenario: Δv for different collision metrics and propulsion systems.

ρ causes the trajectory to fall closer to the semi-major axis, in this case, the maneuver is completely changed. The SCP solver is not assured of finding the global optimum of the original OCP because the found solution could fall in a local optimum well. In fact, counter-intuitively the Δv required by the robust maneuver is lower than the one where the constraint was not applied (37 mm/s vs 51 mm/s). As pointed out in [7], the SOCP can only recover a local optimum solution depending on the initial reference solution. In other words, if a higher-cost solution falls closer to the initial ballistic trajectory, the solver is likely to find it and miss the global optimum. Nonetheless, the solver can still recover the optimal solution that is found in the case where the sensitivity constraint is employed. If the solution of the case with the sensitivity constraint is taken as reference and the SOCP is run without the constraint, the solution found is close to the reference, with a slightly lower Δv , 34 mm/s.

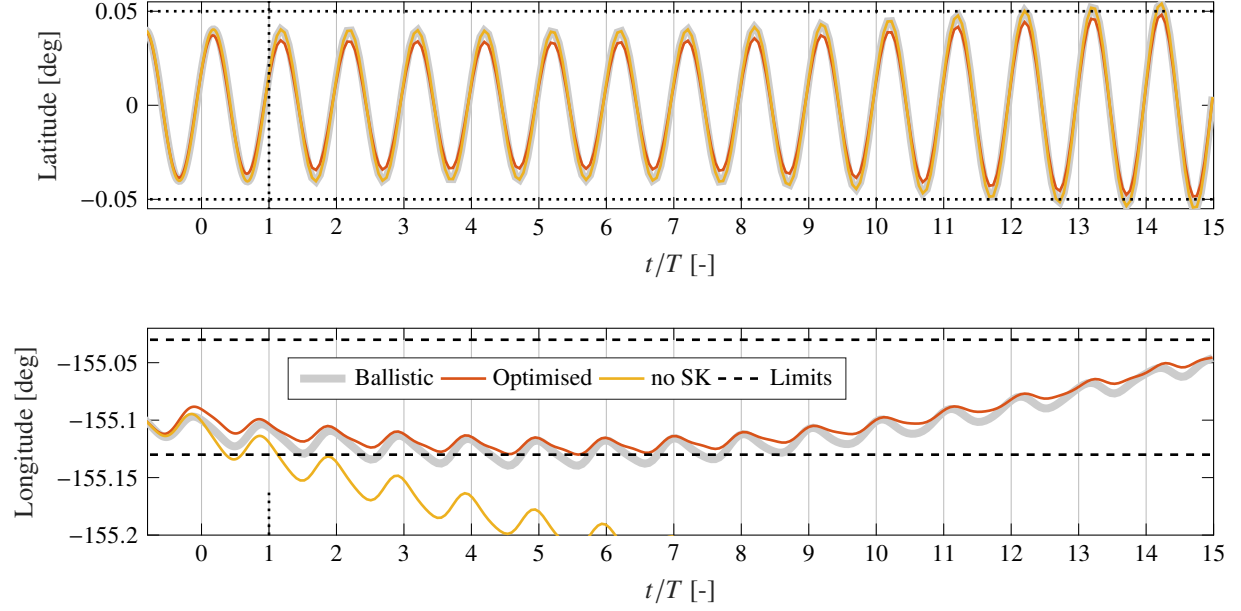
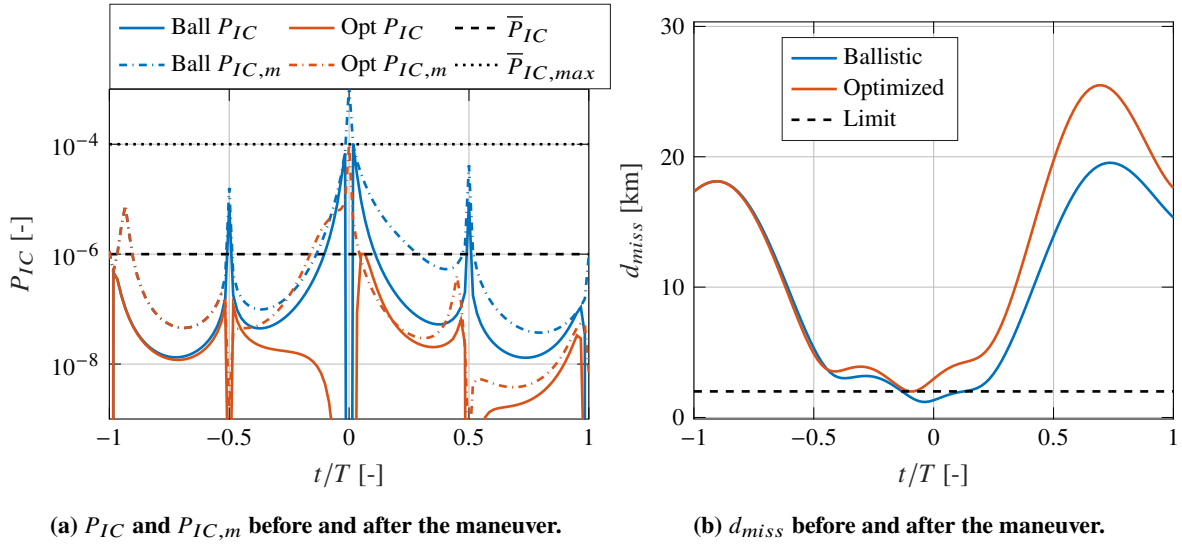


Figure 8 GEO scenario: latitude and longitude evolution with and without the SK requirement.



(a) P_{IC} and $P_{IC,m}$ before and after the maneuver.

(b) d_{miss} before and after the maneuver.

Figure 9 GEO scenario: collision metrics comparison.

C. Convergence and Analysis of the Solutions

This work aimed to develop a reliable and efficient algorithm that converges in a large set of CA scenarios and thus is suitable for autonomous CAMs computation. This section analyzes the convergence properties of the SCP.

In all the simulations presented in this work, the value of $\bar{\nu}$ was 10^{-3} for LEO scenarios and 10^{-4} for GEO ones. These values are low because we expect the CAM to deviate from the original orbit by a small amount; in GEO the value is lower because in absolute terms typically the norm of the Cartesian position is one order of magnitude higher than in LEO. For all the simulations, the tolerance for the convergence of the major iterations $tol_M = 10^{-3}$ and the one for the

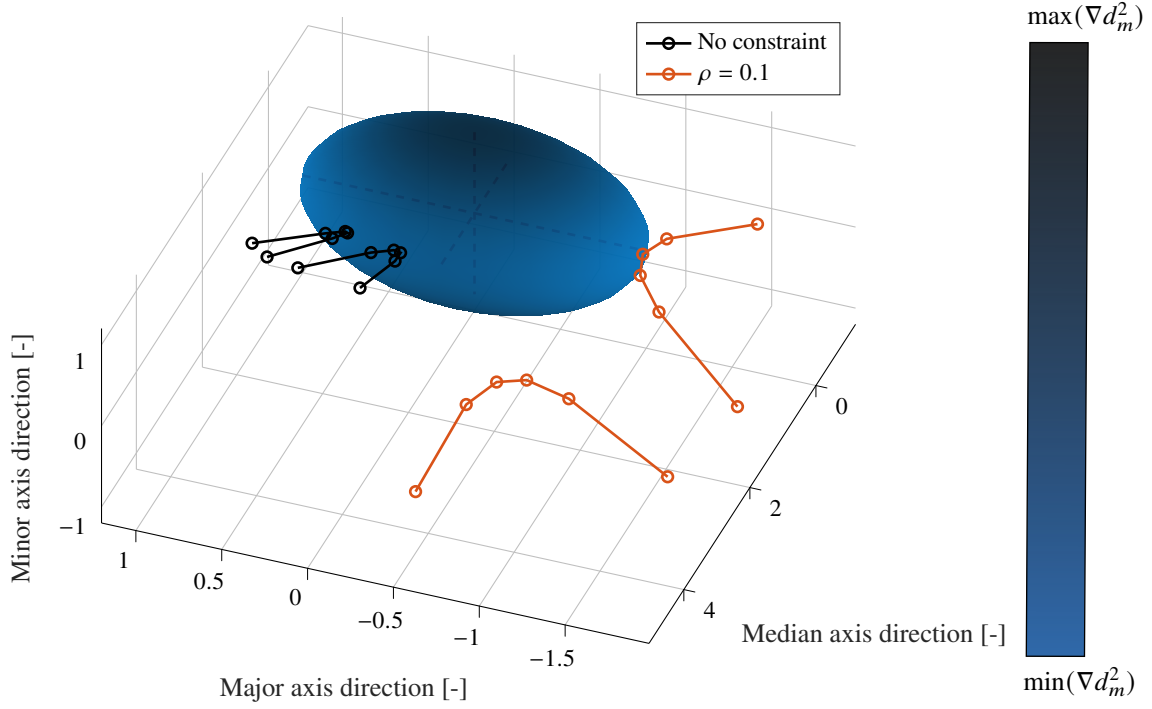


Figure 10 GEO scenario: optimized trajectory in the covariance space.

minor iterations is $tol_m = 10^{-6}$. The major iterations error is computed as the maximum difference between the control action of iteration j and that of iteration $j - 1$. The control action is always normalized w.r.t. the maximum control so that $0 \leq \|u_i\| \leq 1$. In this way, the entity of the error is independent of the maximum control and the major iteration tolerance does not need to be adjusted as a function of u_{max} . The minor iteration error is the maximum difference between the optimized relative position of two consecutive minor iterations. A complementary condition to reach convergence is the minimization of the sum of the virtual controls below a threshold of 10^{-7} , which is achieved in all simulations before the third major iteration.

In Table 5, the convergence results for the test cases analyzed are reported. The number of major iterations used to linearize the dynamics is always kept below 10, showing that the executed maneuvers are typically small and the deviation from the ballistic trajectory is almost negligible on an orbital scale. The trend indicates that the number of iterations is proportional to the length of the propagation window; also, simulations with high thrust systems usually require fewer iterations because the impulsive Δv the control is only active on a limited number of nodes, and the maneuvers are small. Lastly, in LEO, the use of the SK targeting constraint improves the convergence because the first reference solution already satisfies the constraint, whereas the same cannot be observed for GEO cases. The execution time τ is proportional to the number of minor iterations. More than 89% of the run time is required by the linearization of the dynamics and the building of the linear maps; on average, the solution of the convex problem only requires around 10% of the total run time. The implementation of the code is not optimized for speed, and it is the authors' opinion that

Table 5 Convergence properties of the simulations.

sim n	n_{orb} [-]	orbit	SK	Thrust	∇d_m^2	n_{maj} [-]	n_{min} [-]	e [m]	τ [s]
1	2	LEO	No	High	No	5	18	0.013	26.9
2	2	LEO	Yes	High	No	3	7	0.468	16.5
3	2	LEO	No	Low	No	3	11	0.011	17.5
4	2	LEO	Yes	Low	No	5	11	0.146	27.8
5	1	LEO	No	High	No	2	6	0.001	5.4
6	1	LEO	No	High	Yes	4	13	0.008	12.1
7	2	GEO	No	High	No	2	6	0.129	6.9
8	2	GEO	No	Low	No	10	19	0.288	29.8
9	2	GEO	Yes	High	No	2	9	0.080	6.8
10	2	GEO	Yes	Low	No	6	25	0.352	17.8
11	2	GEO	Yes	High	Yes	7	40	0.312	23.6
12	1	GEO	No	High	No	2	6	0.129	7.6
13	1	GEO	No	High	Yes	9	67	0.342	35.7

the time to find a solution could be reduced by one order of magnitude at least.

VII. Conclusions

A sequential convex program (SCP) was developed to design fuel-optimal collision avoidance maneuvers in long-term encounters. The original non-convex optimal control problem is locally approximated into a second-order cone program (SOCP), and the solution is found iteratively. The collision risk is estimated either via the instantaneous probability of collision, the maximum instantaneous probability of collision, or the miss distance. This allows for using the squared Mahalanobis distance (d_m^2) to formulate the collision avoidance constraint as an ellipsoidal keep-out zone. The dynamics are automatically linearized via differential algebra, allowing for any dynamical model in the SCP, e.g., high-order gravitational harmonics, atmospheric drag, solar radiation pressure, and third body attraction. Moreover, the station-keeping operational requirement is introduced as a convex constraint, and a sensitivity constraint on the squared Mahalanobis distance is used to improve the robustness of the maneuver against modeling and actuation errors. A new trust region algorithm based on the nonlinearity index is introduced to avoid artificial unboundedness due to the linearization.

The algorithm is tested on realistic scenarios in GEO and in LEO. The optimizer can recover an optimal solution in all the test cases considered without prior knowledge of the thrust arc structure or thrust direction. It is shown that the computed maneuver can be different when different collision metrics are selected. The algorithm's flexibility allows it to find solutions in high and low-thrust scenarios. The introduction of the novel d_m^2 sensitivity constraint can modify the maneuver significantly, as it constraints the spacecraft on the surface of the keep-out zone where the gradient of d_m^2 is

lower.

The proposed method is proven reliable and efficient, resulting in a promising step towards autonomous collision avoidance maneuver computation.

Funding Sources

The work presented is supported by AOARD under Grant FA2386-21-1-4115.

References

- [1] ESOC, “ESA’s Annual Space Environment Report,” Tech. rep., ESA, 2023.
- [2] Letizia, F., Colombo, C., and Lewis, H. G., “Collision Probability Due to Space Debris Clouds Through a Continuum Approach,” *Journal of Guidance, Control, and Dynamics*, Vol. 39, No. 10, 2015, pp. 2240–2249. <https://doi.org/10.2514/1.G001382>, URL <https://doi.org/10.2514/1.G001382>.
- [3] Zhang, H., Li, Z., Wang, W., Zhang, Y., and Wang, H., “Geostationary Orbital Debris Collision Hazard after a Collision,” *Aerospace*, Vol. 9, No. 258, 2022. <https://doi.org/10.3390/aerospace9050258>, URL <https://doi.org/10.3390/aerospace9050258>.
- [4] Zhang, Y., Li, B., Liu, H., and Sang, J., “An analysis of close approaches and probability of collisions between LEO resident space objects and mega constellations,” *Geo-spatial Information Science*, Vol. 25, No. 1, 2022, pp. 104–120. <https://doi.org/10.1080/10095020.2022.2031313>, URL <https://doi.org/10.1080/10095020.2022.2031313>.
- [5] Browns, A. C., “Human Spaceflight Recent Conjunctions of Interest Human Spaceflight Screening and Notification,” *Proceedings of the USSTRATCOM Conjunction Summary Message Workshop*, 2010, p. 3.
- [6] Hernando-Ayuso, J., and Bombardelli, C., “Low-thrust Collision Avoidance in Circular Orbits,” *Journal of Guidance Dynamics and Control*, 2020.
- [7] Armellin, R., “Collision avoidance maneuver optimization with a multiple-impulse convex formulation,” *Acta Astronautica*, Vol. 186, 2021, pp. 347–362. <https://doi.org/10.1016/j.actaastro.2021.05.046>.
- [8] De Vittori, A., Palermo, M. F., Di Lizia, P., and Armellin, R., “Low-Thrust Collision Avoidance Maneuver Optimization,” *Journal of Guidance, Control, and Dynamics*, Vol. 45, No. 10, 2022, pp. 1815–1829. <https://doi.org/10.2514/1.G006630>.
- [9] Núñez Garzón, U. E., and Lightsey, E. G., “Relating Collision Probability and Separation Indicators in Spacecraft Formation Collision Risk Analysis,” *Journal of Guidance, Control, and Dynamics*, Vol. 45, No. 3, 2022, pp. 517–532. <https://doi.org/10.2514/1.G005744>.
- [10] Chan, K., “Short-term vs long-term spacecraft encounters,” *Collection of Technical Papers - AIAA/AAS Astrodynamics Specialist Conference*, Vol. 3, 2004, pp. 1732–1752.

- [11] Dolado, J. C., Legendre, P., Garmier, R., Revelin, B., and Pena, X., "Satellite collision probability computation for long term encounters," *Advances in the Astronautical Sciences*, Vol. 142, 2012, pp. 275–294.
- [12] Wen, C., and Qiao, D., "Calculating collision probability for long-term satellite encounters through the reachable domain method," *Astrodynamics*, Vol. 6, No. 2, 2022, pp. 141–159. <https://doi.org/10.1007/s42064-021-0119-8>.
- [13] Mueller, J. B., "Onboard Planning of Collision Avoidance Maneuvers Using Robust Optimization," *AIAA Infotech@Aerospace Conference*, Seattle, Washington, 2009.
- [14] Serra, R., Arzelier, D., Joldes, M., Rondepierre, A., Serra, R., Arzelier, D., Joldes, M., Rondepierre, A., Collision, P., Serra, R., Arzelier, D., Joldes, M., and Rondepierre, A., "Probabilistic Collision Avoidance for Long-term Space Encounters via Risk Selection," *Advances in Aerospace Guidance, Navigation and Control*, 2015. URL <https://hal.archives-ouvertes.fr/hal-01995936>.
- [15] Liu, X., Lu, P., and Pan, B., "Survey of convex optimization for aerospace applications," *Astrodynamics*, Vol. 1, No. 1, 2017, pp. 23–40. <https://doi.org/10.1007/s42064-017-0003-8>.
- [16] Dutta, S., and Misra, A. K., "Convex optimization of collision avoidance maneuvers in the presence of uncertainty," *Acta Astronautica*, Vol. 197, 2022, pp. 257–268. <https://doi.org/10.1016/j.actaastro.2022.05.038>.
- [17] Pinson, R., and Lu, P., "Trajectory design employing convex optimization for landing on irregularly shaped asteroids," *Journal of Guidance, Control, and Dynamics*, Vol. 41, No. 6, 2018, pp. 1243–1256. <https://doi.org/10.2514/1.G003045>.
- [18] Alonso-Mora, J., Montijano, E., Ngeli, T., Hilliges, O., Schwager, M., and Rus, D., "Distributed multi-robot formation control in dynamic environments," *Autonomous Robots*, Vol. 43, No. 5, 2019, pp. 1079–1100. <https://doi.org/10.1007/s10514-018-9783-9>.
- [19] Pirovano, L., and Armellin, R., "Maneuver estimation from optical observations of a spiraling orbit: the case of MEV-2," *2022 Advanced Maui Optical and Space Surveillance Technologies Conference (AMOS)*, Maui, Hawaii, 2022. URL www.amostech.com.
- [20] Mueller, J. B., Griesemer, P. R., and Thomas, S. J., "Avoidance maneuver planning incorporating station-keeping constraints and automatic relaxation," *Journal of Aerospace Information Systems*, Vol. 10, No. 6, 2013, pp. 306–322. <https://doi.org/10.2514/1.54971>.
- [21] Vittaldev, V., and Russell, R. P., "Space object collision probability using multidirectional Gaussian mixture models," *Journal of Guidance, Control, and Dynamics*, Vol. 39, No. 9, 2016, pp. 2161–2167. <https://doi.org/10.2514/1.G001610>.
- [22] Armellin, R., Di Lizia, P., Bernelli-Zazzera, F., and Berz, M., "Asteroid close encounters characterization using differential algebra: The case of Apophis," *Celestial Mechanics and Dynamical Astronomy*, Vol. 107, No. 4, 2010, pp. 451–470. <https://doi.org/10.1007/s10569-010-9283-5>.
- [23] Alfried, K. T., Akella, M. R., Frisbee, J., Foster, J. L., Lee, D.-J., and Wilkins, M., "Probability of collision error analysis," *Space Debris*, 2000.

- [24] Coppola, V. T., “Including velocity uncertainty in the probability of collision between space objects,” *AIAA/AAS Astrodynamics Specialist Conference 2014*, Vol. 143, San Diego, California, 2012, pp. 2159–2178.
- [25] Wang, Z., and Grant, M. J., “Minimum-Fuel Low-Thrust Transfers for Spacecraft: A Convex Approach,” *IEEE Transactions on Aerospace and Electronic Systems*, Vol. 54, No. 5, 2018, pp. 2274–2290. <https://doi.org/10.1109/TAES.2018.2812558>.
- [26] Mao, Y., and Acikmese, B., “SCvx-fast: A Superlinearly Convergent Algorithm for A Class of Non-Convex Optimal Control Problems,” *ArXiv*, Vol. 2112, 2021. URL <http://arxiv.org/abs/2112.00108>.
- [27] Malyuta, D., Reynolds, T. P., Szmuk, M., Lew, T., Bonalli, R., Pavone, M., and Acikmese, B., “Convex Optimization for Trajectory Generation,” *ArXiv*, 2021. URL <http://arxiv.org/abs/2106.09125>.
- [28] Losacco, M., Fossà, A., and Armellin, R., “A low-order automatic domain splitting approach for nonlinear uncertainty mapping,” *ArXiv*, 2023.
- [29] Bernardini, N., Wijayatunga, M. C., Baresi, N., and Armellin, R., “State-Dependent Trust Region for Successive Convex Optimization of Spacecraft Trajectories,” *AAS/AIAA Space Flight Mechanics Meeting*, Austin, TX, 2023, pp. 1–20.
- [30] Morselli, A., Armellin, R., Di Lizia, P., and Bernelli Zazzera, F., “A high order method for orbital conjunctions analysis: Sensitivity to initial uncertainties,” *Advances in Space Research*, Vol. 53, No. 3, 2014, pp. 490–508. <https://doi.org/10.1016/j.asr.2013.11.038>, URL <http://dx.doi.org/10.1016/j.asr.2013.11.038>.
- [31] Bombardelli, C., and Hernando-Ayuso, J., “Optimal impulsive collision avoidance in low earth orbit,” *Journal of Guidance, Control, and Dynamics*, Vol. 38, AIAA International, 2015, pp. 217–225. <https://doi.org/10.2514/1.G000742>.
- [32] Pavanello, Z., Pirovano, L., and Armellin, R., “Long-Term Encounters Collision Avoidance Maneuver Optimization with a Multiple-Impulse Convex Formulation,” *AAS/AIAA Space Flight Mechanics Meeting*, Austin, TX, 2023, pp. 1–20.